
# MULTI-MODE ANALYSIS OF
# DUAL RIDGED WAVEGUIDE SYSTEMS
# FOR MATERIAL CHARACTERIZATION

DISSERTATION

Jason G. Crosby, Major, USAF

AFIT-ENG-DS-15-S-011

**DEPARTMENT OF THE AIR FORCE**
**AIR UNIVERSITY**

***AIR FORCE INSTITUTE OF TECHNOLOGY***

**Wright-Patterson Air Force Base, Ohio**

The views expressed in this dissertation are those of the author and do not reflect the official policy or position of the United States Air Force, the Department of Defense, or the United States Government.

AFIT-ENG-DS-15-S-011

# MULTI-MODE ANALYSIS OF DUAL RIDGED WAVEGUIDE SYSTEMS FOR MATERIAL CHARACTERIZATION

DISSERTATION

Presented to the Faculty

Graduate School of Engineering and Management

Air Force Institute of Technology

Air University

Air Education and Training Command

in Partial Fulfillment of the Requirements for the

Degree of Doctor of Philosophy

Jason G. Crosby, BS, MS

Major, USAF

September 2015

AFIT-ENG-DS-15-S-011

# MULTI-MODE ANALYSIS OF DUAL RIDGED WAVEGUIDE SYSTEMS FOR MATERIAL CHARACTERIZATION

Jason G. Crosby, BS, MS
Major, USAF

Committee Membership:

Michael J. Havrilla, PhD
chair

Maj Milo W. Hyde, PhD
member

William P. Baker, PhD
member

Adedeji B. Badiru
Dean, Graduate School of Engineering
and Management

AFIT-ENG-DS-15-S-011


## Abstract

In this dissertation, two nondestructive dual ridged waveguide (DRWG) material characterization systems are investigated. The single and clamped DRWG probe geometries were analyzed in previous work; however, that research only incorporated the dominant DRWG mode. Here, that restriction is removed and the existence of evanescent higher-order modes is considered. Theoretical analysis of the single and clamped DRWG probes is presented and discussed. The approach taken here is similar to that presented in previous research: Love's equivalence theorem is used to remove the DRWG apertures which are replaced with equivalent magnetic currents radiating in the presence of the background parallel-plate waveguide structure. Enforcing the continuity of the tangential magnetic fields in the DRWG and parallel-plate regions yields a system of coupled magnetic field integral equations (MFIEs). This coupled MFIE system is solved using the Method of Moments (MoM) where the tangential electric and magnetic fields in the DRWG are used as expansion and testing functions, respectively. Inversion of the resulting MoM impedance matrix produces theoretical expressions for the reflection and transmission coefficients which are numerically inverted (via nonlinear least squares) to yield estimates of the permittivity and permeability of the material under test. While the steps taken in the theoretical development are similar to previous work, the addition of higher-order modes into the analysis substantially complicates the derivation and is a significant extension of the existing dominant-mode-only literature. Lastly, simulation results of the two structures are presented. A comparison of the dominant-mode only reflection and transmission coefficients with the higher-order mode coefficients is provided.

## Table of Contents

Page

## List of Figures

## List of Tables

## List of Symbols

| Symbol | Definition |
|---|---|
| $\epsilon$ | Electric Permittivity |
| $\mu$ | Magnetic Permeability |
| $k_c$ | Cutoff Wave Number |

*Subscripts*

| | |
|---|---|
| *re* | real component of a complex number |
| *im* | imaginary component of a complex number |
| *x* | x directed field |
| *y* | y directed field |
| *t* | transverse directed field |

*Superscripts*

| | |
|---|---|
| *g* | gap region |
| *r* | right trough region |
| *l* | left trough region |
| 1 | first waveguide (centered around origin) |
| 2 | second waveguide |

*indices*

| | |
|---|---|
| *n* | gap expansion index |
| *m* | trough expansion index |
| $\tilde{n}$ | gap testing index |
| $\tilde{m}$ | trough testing index |

## List of Acronyms

| Acronym | Definition |
|---|---|
| DRWG | dual ridged waveguide |
| MUT | material under test |
| PEC | perfect electric conductor |
| VP | vector potential |
| PEC | perfect electrical conductor |
| NDE | nondestructive evaluation |
| USAF | United States Air Force |
| NRW | Nicholson-Ross-Weir |

MULTI-MODE ANALYSIS OF
DUAL RIDGED WAVEGUIDE SYSTEMS
FOR MATERIAL CHARACTERIZATION

# I. Introduction

## 1.1 Introduction

Electromagnetic material characterization is the process of determining the dielectric, magnetic, and magnetoelectric properties of a material. For simple (i.e., linear, homogeneous and isotropic) media, which is the focus of this research, these properties are the permittivity $\epsilon = \epsilon_{re} + j\epsilon_{im}$ and permeability $\mu = \mu_{re} + j\mu_{im}$. In general, material characterization is classified as destructive or nondestructive. In destructive techniques, the material under test (MUT) is machined or altered in some way in order to fit into the electromagnetic testing device (e.g., waveguide). Destructive techniques often have the significant advantage of allowing extraction of the permittivity and permeability of a MUT via simple closed-form analytic expressions which are computationally efficient (e.g., 1-2 seconds). However, since destructive techniques require the MUT to be cut to fit inside the test device, significant errors can be introduced if sample fit is not perfect. In contrast, a nondestructive process seeks to determine material parameters without altering the shape of the MUT. Thus, sample fit problems are mitigated and substantial time is saved in not having to perform any sample preparation. In addition, nondestructive techniques have the benefit to be utilized in the field as point inspection tools. The drawback of nondestructive techniques is that the measurement environment is substantially more complex, thus computationally-intensive iterative algorithms are required to extract permittivity and permeability values of the MUT. Due to the intended purpose of developing flight-line

testing tools, the focus of this research will be on nondestructive evaluation of simple media. While many choices for nondestructive evaluation (NDE) exist, this research will focus and expand upon prior research using Dual Ridged Waveguide (DRWG) probes.

## 1.2 Problem Statement

NDE of material parameters has always been important to the United States Air Force (USAF). Material coatings are predominant on many air vehicles to manage radar detectability, thus material characterization on the flight line plays a crucial role in vehicle health performance and maintenance. Since these material coatings are physically adhered to the vehicle body (i.e., metallic conductor), nondestructive techniques are required to assess permittivity and permeability data, and thus, the radar reducing performance metrics. In order to accurately locate and detect permittivity and permeability changes in the aircraft material coating, NDE test fixtures having large bandwidth are desirable due to enhanced resolution. Current techniques, namely single and double rectangular waveguide probes used to characterize perfect electrical conductor (PEC) backed material, lack appropriate bandwidth. A clamped rectangular waveguide technique useful in laboratory environment also exists, but cannot be utilized for characterizing conductor-backed materials and suffers the same bandwidth limitation.

The primary goals of this research effort are to replace the existing rectangular waveguide probes (single, double and clamped) with dual-ridged waveguide components. The dramatic benefit of using dual-ridged waveguides is a three-fold improvement in bandwidth (and hence, three-fold improvement in resolution). This effort will build upon other work related to dual-ridged waveguides, namely, single and clamped probe research performed by [19, 20], which considered dominant-mode propagation only. The investigation here considers the existence of higher-order modes in the dual-ridged waveguides and how they influence the accuracy of extracted permittivity and permeability values. This is a critical issue since the inclusion of higher-order modes can add substantial

time to the material property extraction process, namely, from several minutes for the dominant mode to several days for the inclusion of several higher-order modes. Obviously, a material extraction process that takes several days is quite useless for the high demands of a flight line. If it can be shown that the higher-order modes do not significantly contribute to accuracy, than the dual-ridged waveguide can be considered a valuable and time-efficient diagnostic tool, at least for the class of materials typically encountered in flight-line environments. In addition to the use of DRWG's for single and clamped probes, a double (i.e., dual) probe geometry will also be investigated. The dual probe dual-ridged waveguide test fixture has the advantage of being able to acquire both reflection and transmission data, which is important in material characterization since these quantities are linearly independent.

Investigation of literature reveals that the development of the dual probe DRWG system as well as higher order mode expansion of the single and clamped dual-ridged systems represent original work. They also have the potential of being considered as significant contributions as mentioned above, especially for flight-line applications. This research may also lead to better, more accurate, NDE techniques for broader classes of media.

### 1.3 Material Characterization Background and Methods

It is important to understand the benefits of accurate NDE of materials. As advancements in materials and material manufacturing are made, accurate characterization is important for the intended application. As one colleague wrote, "when producing a material, how do you know you made what you wanted to make?" [30]. Without being able to confirm a material's properties, it would not be possible to accurately model new designs such as antennas and absorbing coatings. While many numerous techniques exist in the microwave spectrum, their effectiveness varies. Material type, models used, frequency

range, and lab set-up all play a role in determining which technique is most effective. This section presents a short review of several techniques involving waveguides.

### *1.3.1 Coaxial Waveguides.*

Coaxial waveguides are very common due to their bandwidth and information-carrying capabilities. These waveguides consist of an inner conductor surrounded by insulation which is further surrounded by an outer conductor sometimes referred to as a shield. This is further surrounded by another layer of protective insulation. A picture of a generic coaxial cable structure is shown in Figure (1.1). These cables are generally round and flexible and are commonly used for material characterization when the region between the inner and outer conductors is air filled (center conductor held into position by small/thin teflon dielectric beads).

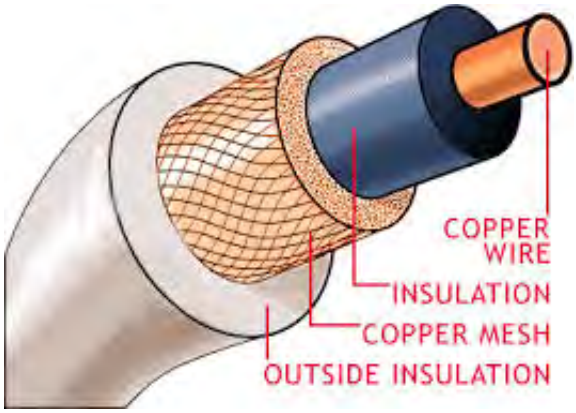


Figure 1.1: Coaxial cable structure.

Coaxial probes have been used in many applications [2–4, 6, 8, 11, 12, 17, 25, 29, 32, 36]. While they provide the potential for broadband measurements, these systems depend greatly on the MUT and waveguide size in order to obtain accurate material properties [11, 12]. Many of these references discuss that, although the theoretical bandwidth of a commonly-used 7mm coax is 18 GHz, the effective bandwidth for accurate material

characterization is only about 10 GHz due to the field structure and lack of bore-site field coupling into the material under test, especially at lower frequencies. It has also been shown that field penetration is better in lossy material when compared to lowloss materials, again due to field structure and the types of currents that can exist in these types of materials.

### *1.3.2 Rectangular and Circular Waveguides.*

Rectangular and circular waveguides are much more physically robust than coaxial waveguides. There construction is also much simpler being a simple rectangular or circular tube constructed of a material with near PEC properties. A rectangular and circular waveguide are shown in Figure (1.2).

Figure 1.2: Rectangular and circular waveguide.

Rectangular and circular waveguides have also been used in many applications [7, 9, 18, 19, 23, 24, 26, 31, 34]. In addition to there robustness, rectangular and circular waveguides do not have the coupling problems previously noted for coaxial waveguides. They also have very simple field expressions in terms of elementary functions (sines, cosines, exponentials and Bessel functions) and corresponding propagation constants of the allowed modes can be found in closed form. The primary drawback of these test fixtures is that they are band limited. As an example, an air-filled X-band waveguide (having cross-sectional dimensions of 2.286 cm by 1.016 cm) has a bandwidth of only 4 GHz when operated in the traditional dominant-mode configuration.

### *1.3.3 DRWGs.*

DRWGs are somewhat similar to rectangular waveguides in construction. They resemble a rectangular waveguide with a ridge on the long sides (typically considered the $x$ axis) of the waveguide. This gives the waveguide the shape of an H. Figure 2.1 shows a cross-sectional depiction of a dual ridge waveguide (single ridge waveguides are also common, but are not investigated here due to their limited bandwidth). Originally developed in [27], these waveguides have the benefit of robustness of a solid waveguide and a three-fold increase in bandwidth over a similar rectangular waveguide. However, the field expressions are more complicated as a result of the three distinct regions (i.e., separate field expressions for each region). In addition, the allowed propagation constants must be found numerically, leading to reduced computational efficiency. Recent research efforts have been conducted on single probe DRWG systems [21] as well as clamped systems [20] showing the ability to accurately characterize simple materials with approximately 3 times the bandwidth of a traditional X-band waveguide.

### *1.3.4 Single Probe Waveguide Systems.*

A single probe system uses only a single waveguide to characterize a material. The waveguide can be of any type previously discussed. A single probe waveguide

system is one of the subjects for this research and an example can be seen in Chapter 3. While numerous papers have been published on single probe waveguide systems [7–9, 11, 12, 17, 18, 25, 26, 29, 31, 32, 34, 36], a single probe system cannot easily determine both complex permittivity and permeability. This is because the system can only take a single measurement (i.e., reflection measurement) allowing for calculation of a single unknown. Several techniques have been developed to alleviate this problem such as two thickness method [9, 10, 26, 33], two layer method [3, 14, 26, 34], frequency varying method [26, 35], free space backed method [3, 25, 34], and two iris method [13]. However, these techniques have disadvantages such as instability (two layer method), physically difficult to measure (free space backed method), require prior knowledge of the MUT (two thickness and frequency varying methods), or require two waveguides (two iris method)[20]. As mentioned previously, the accommodation of higher-order modes in a dual-ridged single probe waveguide for the purpose of enhancing material property extraction is investigated as part of this research effort, and is discussed in Chapter 3.

#### *1.3.5 Two Probe Waveguide Systems.*

A two probe system uses two separate waveguides typically in a clamped [2, 24] or dual [6, 23] configuration. The waveguide can be of any type previously discussed. Dual-ridged waveguide dual probe and clamped systems are the remaining effort of this research and are discussed further in Chapters 2 and 4, respectively. As noted previously, two probe systems are desirable because they can make multiple independent measurements (typically reflection and transmission) and thus determine both permittivity and permeability simultaneously.

## 1.4 Assumptions

The following established assumptions (e.g., [30]) are used in this research.

- An $e^{j\omega t}$ time dependence is assumed and suppressed throughout.

- The transverse axes are $x$ and $y$ and the direction of propagation is the $z$ axis.
- Conducting surfaces, such as the waveguide walls and parallel plates, are assumed to be a PEC.
- The transverse dimensions of the material sample and parallel plates are assumed to be infinite in extent.
- The DRWG's contain only free space with material parameters $\epsilon_0$ and $\mu_0$.
- The MUT is simple (linear, isotropic, homogeneous), and the sample has a uniform thickness.
- The waveguide probes are perfectly aligned in all dimensions.

## 1.5 Overview and Organization

This chapter has provided the background and motivation for this research. Several NDE techniques were briefly discussed along with previous work on the subject. Goals for this research as well as how this research will impact the USAF was presented. Chapter 2 will discuss the dual probe DRWG system development. Chapters 3 and 4 will cover higher order expansion of the single probe system and clamped probe systems, respectively. Finally, Chapter 5 will present conclusions of this work and suggest future research areas.

# II. Dual Probe DRWG

In this chapter, the analysis of a dual probe dual-ridged waveguide (DRWG), shown in Figures 2.1 and 2.2, is performed. The analysis includes an examination of the reflection and transmission (i.e., coupling) coefficients of the dual probe DRWG placed on a conductor-backed material. It is assumed in the analysis that only a single dominant mode is propagating in the free-space filled DRWG's. Two simulation scenarios are considered, namely, a lossy and low loss conductor-backed material. The fundamental goal for performing this analysis is to assess if this probe has sufficient sensitivity to simultaneously extract permittivity and permeability of the material, and thus, comprise a valuable flight-line diagnostic tool. This can be answered through the investigation of the reflection and transmission coefficient amplitudes. Recall, if two material properties are desired, then two linearly-independent measurements are required (in this case, reflection and transmission coefficients). However, it is also necessary that the measured coefficients have sufficient signal-to-noise ratio. The dual probe analysis aims to answer this critical question. It is intuitively expected for the lossy case that transmission should be maximized (which is desired) when dual probe separation is minimized due to energy absorption in the conductor-backed material as well as wave spreading. However, will minimized probe spacing be sufficient for traditional radar absorbing materials? The intended analysis will answer this critical question. In regards to lossless or low loss media, is minimized probe spacing necessarily desired? The analysis that follows will demonstrate that this is not necessarily true for this case.

The dual probe DRWG analysis will begin with a brief review of the dual-ridged waveguide field expressions. Field plots of the dominant mode is provided, to demonstrate why sufficient transmission coupling is a concern. Next, the fields in the parallel-plate region of the dual probe DRWG are found with the aid of Love's Equivalence Theorem.

Subsequent enforcement of tangential boundary conditions at the dual probe DRWG apertures leads to coupled magnetic field integral equations (MFIE's) for the unknown reflection and transmission coefficients. These MFIE's are solved via the Method-of-Moments for both a lossy and low loss material. Details of the complex-plane analysis utilized in the solution process are included for the benefit of the reader. Simulation results for the reflection and transmission coefficients of both materials are presented and discussed, and general conclusions are provided.

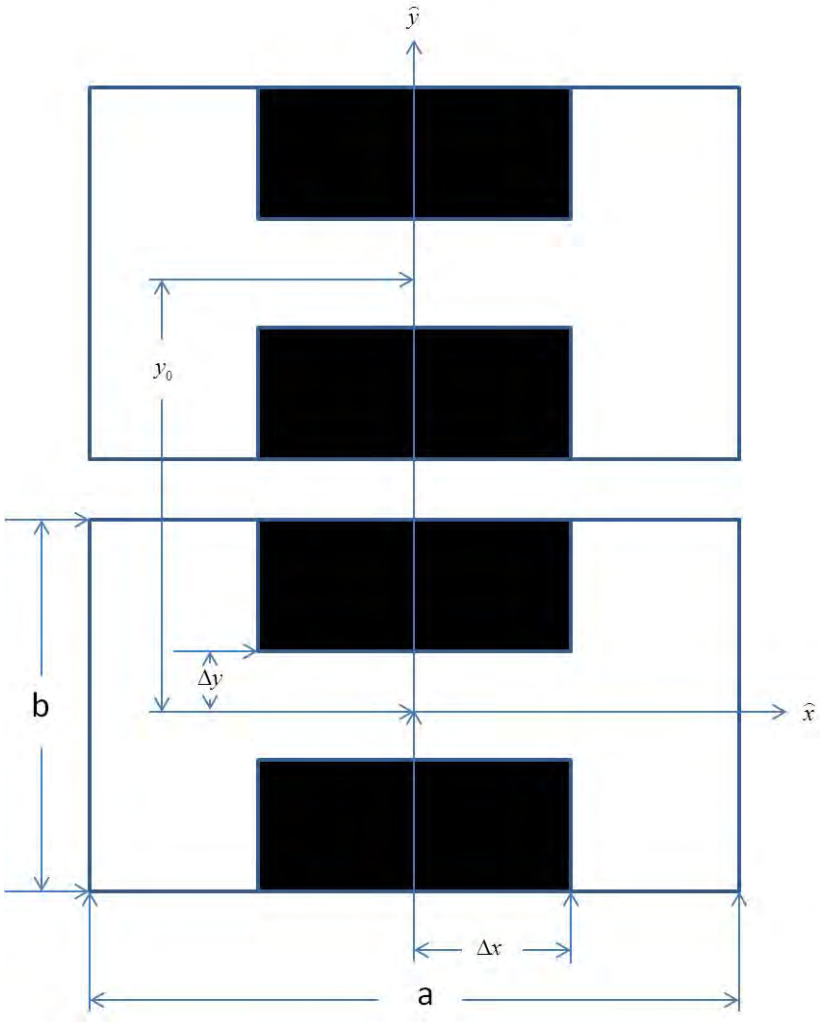


Figure 2.1: Cross-sectional view of dual probe DRWG geometry

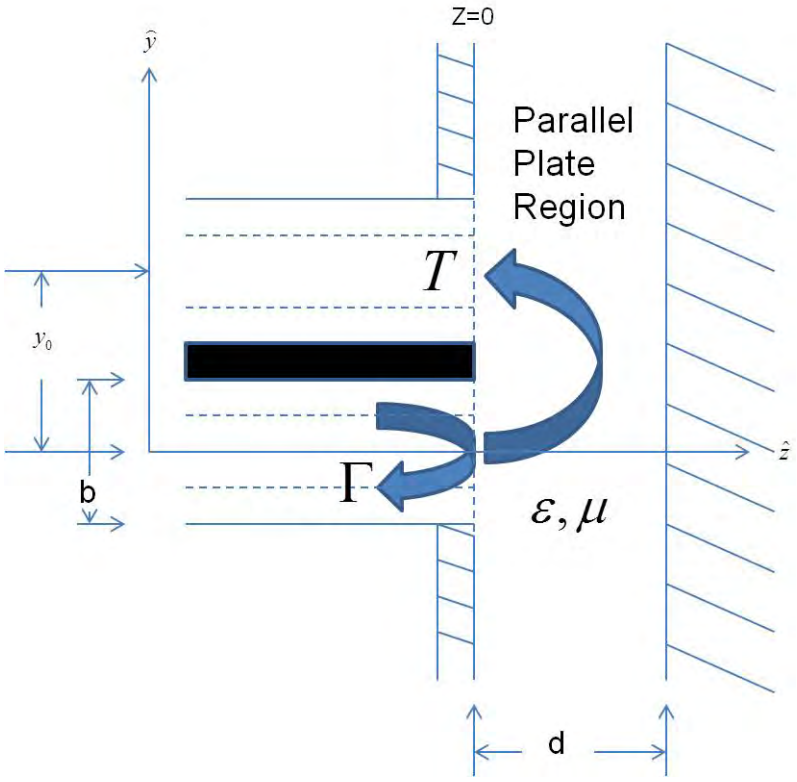


Figure 2.2: Side view of dual probe DRWG geometry

## 2.1 DRWG Fields

Figure 2.1 shows the cross-sectional view of the free-space filled dual probe DRWG, with each DRWG comprised of a right trough region ($\Delta x<x<$a/2,-b/2$<y<$b/2), a central gap region (-$\Delta x<x<\Delta x$,-$\Delta y<y<\Delta y$), and left trough region (-a/2$<x<$-$\Delta x$,-b/2$<y<$b/2). Figure 2.2 depicts the side view of the dual probe DRWG in contact with the conductor-backed material having permittivity $\epsilon$, permeability $\mu$ and occupying the parallel-plate region $z$=0 to $z$=d. It is also assumed that the adjacent DRWG's are located a distance of $y_0$ apart from center to center.

The following desired fields for a DRWG were derived in [15, 27]. These fields are required and used throughout this research as the fields in the DRWG regions of all the DRWG systems.

The $TE^z$ transverse DRWG field expressions are given by

$$\begin{aligned} E_x^g &= \sum_n e_{xn}^g \left[(\beta_n - \alpha_n)\cos(k_{xn}^g x) + (\beta_n + \alpha_n)\sin(k_{xn}^g x)\right]\sin\left(k_{yn}^g(y-\Delta y)\right) \\ E_y^g &= -\sum_n e_{yn}^g \left[(\beta_n - \alpha_n)\sin(k_{xn}^g x) - (\beta_n + \alpha_n)\cos(k_{xn}^g x)\right]\cos\left(k_{yn}^g(y-\Delta y)\right) \\ \overrightarrow{e}_t^g &= \hat{x}E_x^g + \hat{y}E_y^g \\ \overrightarrow{h}_t^g &= \frac{\hat{z}\times\overrightarrow{e}_t^g}{Z^{TE}} \end{aligned} \tag{2.1}$$

in the $|x| < \Delta x$ (gap) subregion,

$$\begin{aligned} E_x^{rt} &= \sum_{n,m} \alpha_n e_{xn,m}^t cos\left[k_{xm}^t\left(\frac{a}{2}-x\right)\right]\sin\left(k_{ym}^g(y-\frac{b}{2})\right) \\ E_y^{rt} &= \sum_{n,m} \alpha_n e_{yn,m}^t sin\left[k_{xm}^t\left(\frac{a}{2}-x\right)\right]\cos\left(k_{ym}^g(y-\frac{b}{2})\right) \\ \overrightarrow{e}_t^{rt} &= \hat{x}E_x^{rt} + \hat{y}E_y^{rt} \\ \overrightarrow{h}_t^{rt} &= \frac{\hat{z}\times\overrightarrow{e}_t^{rt}}{Z^{TE}} \end{aligned} \tag{2.2}$$

in the $x > \Delta x$ (right) trough subregion, and

$$\begin{aligned} E_x^{lt} &= -\sum_{n,m} \beta_n e_{xn,m}^t cos\left[k_{xm}^t\left(\frac{a}{2}-x\right)\right]\sin\left(k_{ym}^g(y-\frac{b}{2})\right) \\ E_y^{lt} &= \sum_{n,m} \beta_n e_{yn,m}^t sin\left[k_{xm}^t\left(\frac{a}{2}-x\right)\right]\cos\left(k_{ym}^g(y-\frac{b}{2})\right) \\ \overrightarrow{e}_t^{lt} &= \hat{x}E_x^{lt} + \hat{y}E_y^{lt} \\ \overrightarrow{h}_t^{lt} &= \frac{\hat{z}\times\overrightarrow{e}_t^{lt}}{Z^{TE}} \end{aligned} \tag{2.3}$$

in the $x < -\Delta x$ (left) trough subregion. In the above field expressions, $Z^{TE} = \omega\mu_0/k_z$ is the $TE^z$ wave impedance and

$$\begin{aligned} e_{xn}^g &= \frac{k_{yn}^g}{2k_{xn}^g cos(k_{xn}^g \Delta x)} \\ e_{yn}^g &= \frac{1}{2cos(k_{xn}^g \Delta x)} \\ e_{xn,m}^t &= \frac{k_{ym}^t \psi_{m,n}}{k_{xm}^t \frac{b}{2}(1+\delta_{m0})sin[k_{xm}^t(\frac{a}{2}-\Delta x)]} \\ e_{yn,m}^t &= \frac{\psi_{m,n}}{\frac{b}{2}(1+\delta_{m0})sin[k_{xm}^t(\frac{a}{2}-\Delta x)]} \end{aligned} \tag{2.4}$$

where

$$\psi_{m,n} = \frac{1}{2}\left(\frac{1}{k_{yn}^{g} - k_{ym}^{t}} - \frac{1}{k_{yn}^{g} + k_{ym}^{t}}\right) \left[sin\left[k_{ym}^{t}\left(\frac{b}{2} - \Delta y\right)\right] - (-1)^{n} sin\left[k_{ym}^{t}\left(\frac{b}{2} - \Delta y\right)\right]\right] \tag{2.5}$$

Variables $k_{ym}^{t} = m\pi/b$ and $k_{yn}^{g} = n\pi/2\Delta y$ are the $y$-directed DRWG wavenumbers in the trough and gap subregions, respectively; $k_{xm}^{t}$ and $k_{xm}^{g}$ are the $x$-directed DRWG wavenumbers in the trough and gap subregions, respectively; and $\alpha_n$ and $\beta_n$ are the complex $TE^z$ modal amplitudes. Note that $k_z = \sqrt{k_0^2 - k_c^2} = \sqrt{k_0^2 - (k_{ym}^{t}) - (k_{xm}^{t})} = \sqrt{k_0^2 - (k_{yn}^{g}) - (k_{xn}^{g})}$ where $k_0 = \omega\sqrt{\epsilon_0\mu_0}$ and $\omega$ is the radian frequency.

The modal plots of the transverse electric field distribution for the dominant mode of the DRWG is shown in Figure 2.3. It is critical to note that the dominant mode is tightly confined to the central gap region. This is of great concern because the effective spacing between the adjacent DRWG's energy concentration in the dual probe system is substantially farther apart than in a rectangular waveguide dual probe configuration. Thus, the main question becomes is there sufficient transmission coupling between the DRWG's for both a lossy and low loss material. The goal of this chapter is to answer that critical concern.

## 2.2 Dual Probe DRWG Region Fields

As a wave travels down the first (centered about the origin) DRWG and interacts with the boundary between the waveguide and the MUT, a portion of the energy will be reflected back into the waveguide [5]. A portion of the energy will also be transmitted into waveguide 2 (offset $y_0$ about the origin). Thus we must first find the total fields in the DRWG regions. Total fields in the DRWG portion of the system are found using the DRWG fields reviewed in section 2.1. Note however, that because of the offset in the $y$ direction a shift is applied to the fields in the second waveguide. Thus the $y$ variation of each field component has

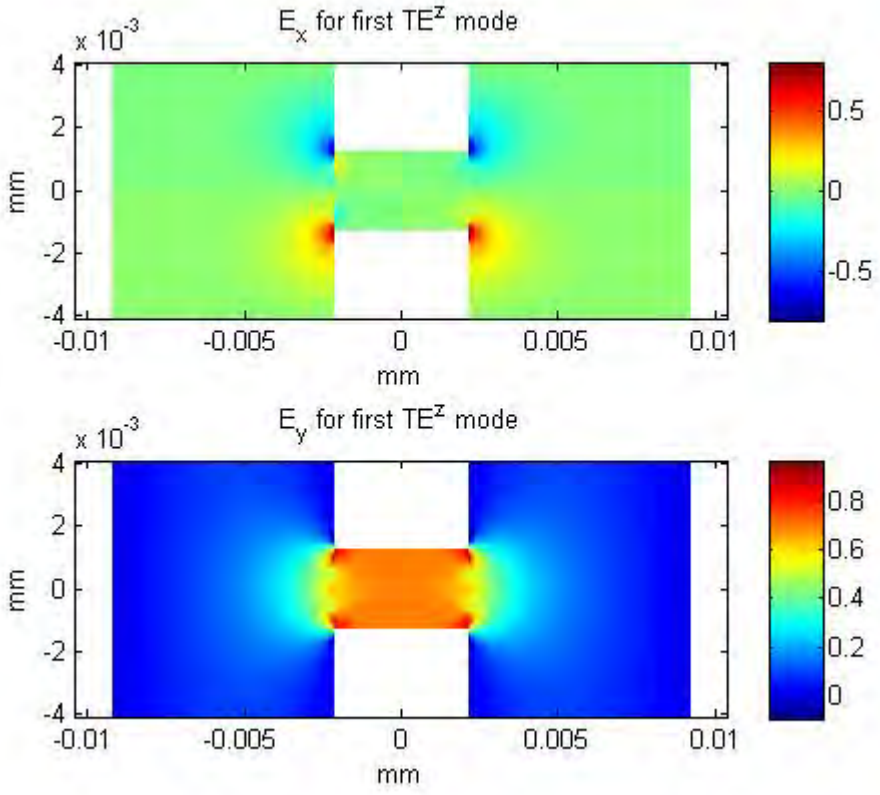


Figure 2.3: Dominant mode transverse electric field distribution.

a form similar to $sin[k_{ym}^{g}(y - (y_0 + \Delta y))]$ where the shift is given by $y_0$. Allowing for this yields fields in the form of

$$\overrightarrow{E}^{1}_{tDRWG} = \left(e^{-jk_z z} + \Gamma e^{jk_z z}\right)\overrightarrow{e}^{1}_{t}(\overrightarrow{\rho}) \tag{2.6}$$

$$\overrightarrow{H}^{1}_{tDRWG} = \left(e^{-jk_z z} - \Gamma e^{jk_z z}\right)\overrightarrow{h}^{1}_{t}(\overrightarrow{\rho}) \tag{2.7}$$

$$\overrightarrow{E}^{2}_{tDRWG} = \mathrm{T}e^{jk_z z}\overrightarrow{e}^{2}_{t}(\overrightarrow{\rho}) \tag{2.8}$$

$$\overrightarrow{H}^{2}_{tDRWG} = -\mathrm{T}e^{jk_z z}\overrightarrow{h}^{2}_{t}(\overrightarrow{\rho}) \tag{2.9}$$

where $\Gamma$ and T are the unknown (i.e., to be determined) reflection and transmission coefficients, respectively. Note, superscripts 1 and 2 denote waveguide 1 and 2.

## 2.3 Parallel Plate Region Fields

As mentioned previously, a wave traveling down the DRWG interacts with the interface between the waveguide and the MUT, causing a portion of the energy to be transmitted into the MUT (i.e., parallel plate field region). This energy gives rise to electromagnetic fields inside the PP region of the system. To determine these fields, first Love's equivalence principle [5] is used to replace the DRWG aperture fields with an equivalent source in the form of magnetic surface currents, namely [5]

$$\vec{M}_1 = -\hat{n} \times \vec{E}_1. \tag{2.10}$$

$$\vec{M}_2 = -\hat{n} \times \vec{E}_2. \tag{2.11}$$

where $\hat{n}$ is the normal unit vector pointing into the MUT region, with $\vec{E}_1$ and $\vec{E}_2$ to be determined. This equivalent system is shown in Figure (2.4). These aperture currents are located at $z = 0$ and occupy the aperture field regions as discussed in section 2.1.

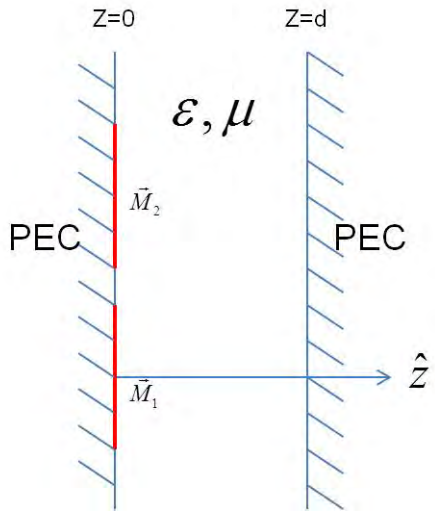


Figure 2.4: Equivalent system for parallel plate region of the dual probe DRWG system after Love's Equivalence Theorem is applied.

Now that the equivalent currents have been identified, a Vector Potential (VP) solution is used to find the parallel plate region magnetic field. This solution is as follows [5]:

$$\overrightarrow{H}_t^{pp}(\overrightarrow{\rho},z) = \frac{1}{j\omega\epsilon\mu}(k^2\underline{I}_t + \nabla_t\nabla\cdot)\overrightarrow{F}_t^{pp}(\overrightarrow{\rho},z). \tag{2.12}$$

where $\underline{I}_t = \hat{x}\hat{x} + \hat{y}\hat{y}$, and $k^2 = \omega^2\epsilon\mu$. However, the $\overrightarrow{F}$ VP must first be identified. The surface currents $\overrightarrow{M}_1$ and $\overrightarrow{M}_2$ support this VP through the following relation,

$$\begin{aligned}\overrightarrow{F}_t^{pp}(\overrightarrow{\rho},z) = &\iint_{S_1}\underline{G}(\overrightarrow{\rho},z|\overrightarrow{\rho}',0)\cdot\epsilon\overrightarrow{M}_1(\overrightarrow{\rho}')ds' \\ &+\iint_{S_2}\underline{G}(\overrightarrow{\rho},z|\overrightarrow{\rho}',0)\cdot\epsilon\overrightarrow{M}_2(\overrightarrow{\rho}')ds'\end{aligned} \tag{2.13}$$

where $\underline{G}(\overrightarrow{\rho},z|\overrightarrow{\rho}',0)$ is the parallel plate Green's function to be discussed in the next section, and $\overrightarrow{M}_1$ and $\overrightarrow{M}_2$ are found using equations 2.10 and 2.11, respectively. Note, $S_1$ and $S_2$ are the DRWG aperture regions as previously discussed. Equating the tangential magnetic field at the apertures leads to the coupled MFIE's

$$\frac{1}{j\omega\epsilon\mu}(k^2\underline{I}_t + \nabla_t\nabla\cdot)\overrightarrow{F}_t^{pp}(\overrightarrow{\rho},z) = (1-\Gamma)\overrightarrow{h}_t^1(\rho). \tag{2.14}$$

$$\frac{1}{j\omega\epsilon\mu}(k^2\underline{I}_t + \nabla_t\nabla\cdot)\overrightarrow{F}_t^{pp}(\overrightarrow{\rho},z) = -\mathrm{T}\overrightarrow{h}_t^2(\rho) \tag{2.15}$$

These MFIEs are solved in the next section via the MoM.

## 2.4 Solving the MFIEs

This section details the solution of the MFIE's of the previous section. The first step of the MoM is to expand the unknown currents ($\overrightarrow{M}_1$) and ($\overrightarrow{M}_2$) in a series of basis functions. In this case we will exploit the fact that we know the transverse electric fields in the DRWG region at $z = 0^-$, and we know that these transverse fields must be continuous across the boundaries at $z = 0^+$, thus we can approximate the equivalent magnetic currents as

$$\overrightarrow{M}_1(\overrightarrow{\rho}') = -\hat{n}\times\overrightarrow{E}_1 \approx -\hat{n}\times\overrightarrow{E}_{tDRWG}^1. \tag{2.16}$$

$$\overrightarrow{M}_2(\overrightarrow{\rho}') = -\hat{n} \times \overrightarrow{E}_2 \approx -\hat{n} \times \overrightarrow{E}^2_{tDRWG}. \tag{2.17}$$

Substitution of 2.16 and 2.17 into 2.13 and further insertion into 2.14 and 2.15 yields the following relations:

$$\frac{1}{j\omega\mu}(k^2 \underline{I}_t + \nabla_t \nabla \cdot) \left[ \iint_{S_1} \underline{G}(\overrightarrow{\rho}, z|\overrightarrow{\rho}', 0) \cdot \overrightarrow{M}_1(\overrightarrow{\rho}') ds' + \iint_{S_2} \underline{G}(\overrightarrow{\rho}, z|\overrightarrow{\rho}', 0) \cdot \overrightarrow{M}_2(\overrightarrow{\rho}') ds' \right] = (1 - \Gamma) \overrightarrow{h}^1_t(\overrightarrow{\rho}) \tag{2.18}$$

$$\frac{1}{j\omega\mu}(k^2 \underline{I}_t + \nabla_t \nabla \cdot) \left[ \iint_{S_1} \underline{G}(\overrightarrow{\rho}, z|\overrightarrow{\rho}', 0) \cdot \overrightarrow{M}_1(\overrightarrow{\rho}') ds' + \iint_{S_2} \underline{G}(\overrightarrow{\rho}, z|\overrightarrow{\rho}', 0) \cdot \overrightarrow{M}_2(\overrightarrow{\rho}') ds' \right] = -\mathrm{T} \overrightarrow{h}^2_t(\overrightarrow{\rho}) \tag{2.19}$$

Next, both sides of equations 2.18 and 2.19 are tested with the complex conjugate of the magnetic field. The testing operators are as follows:

$$\iint_{S_1} \{\cdots\} \cdot \overrightarrow{h}^{1*}_t dS_1 \tag{2.20}$$

$$\iint_{S_2} \{\cdots\} \cdot \overrightarrow{h}^{2*}_t dS_2 \tag{2.21}$$

for 2.18 and 2.19, respectively. After testing, 2.18 and 2.19 become

$$\begin{aligned} \iint_{S_1} \left( \frac{1}{j\omega\mu}(k^2 \underline{I}_t + \nabla_t \nabla \cdot) \left[ \iint_{S_1} \underline{G}(\overrightarrow{\rho}, z|\overrightarrow{\rho}', 0) \cdot \overrightarrow{M}_1(\overrightarrow{\rho}') ds' \right. \right. \\ \left. \left. + \iint_{S_2} \underline{G}(\overrightarrow{\rho}, z|\overrightarrow{\rho}', 0) \cdot \overrightarrow{M}_2(\overrightarrow{\rho}') ds' \right] \right) \cdot \overrightarrow{h}^{1*}_t dS_1 \\ = \iint_{S_1} \left( (1 - \Gamma) \overrightarrow{h}^1_t(\overrightarrow{\rho}) \right) \cdot \overrightarrow{h}^{1*}_t dS_1 \end{aligned} \tag{2.22}$$

$$\begin{aligned} \iint_{S_2} \left( \frac{1}{j\omega\mu}(k^2 \underline{I}_t + \nabla_t \nabla \cdot) \left[ \iint_{S_1} \underline{G}(\overrightarrow{\rho}, z|\overrightarrow{\rho}', 0) \cdot \overrightarrow{M}_1(\overrightarrow{\rho}') ds' \right. \right. \\ \left. \left. + \iint_{S_2} \underline{G}(\overrightarrow{\rho}, z|\overrightarrow{\rho}', 0) \cdot \overrightarrow{M}_2(\overrightarrow{\rho}') ds' \right] \right) \cdot \overrightarrow{h}^{2*}_t dS_2 \\ = - \iint_{S_2} \left( \mathrm{T} \overrightarrow{h}^2_t(\overrightarrow{\rho}) \right) \cdot \overrightarrow{h}^{2*}_t dS_2 \end{aligned} \tag{2.23}$$

It is desirable to use a spectral representation of the Green's function. This representation allows easy evaluation of the spacial integrals involving $x, x', y, y'$, resulting in simple trigonometric functions as shown later. However, it does add two more integral dimensions over spectral variables $\eta$ and $\xi$. The spectral representation of the Green's function is shown below

$$\underline{G}(\overrightarrow{\rho}, z|\overrightarrow{\rho}', 0) = \frac{1}{(2\pi)^2} \iint_{-\infty}^{\infty} \widetilde{\underline{G}_1}(\overrightarrow{\lambda}, z|0) e^{j\xi(x-x')} e^{j\eta(y-y')} d\xi d\eta \tag{2.24}$$

where

$$\overrightarrow{\lambda} = \hat{x}\xi + \hat{y}\eta \tag{2.25}$$

and

$$\widetilde{\underline{G}}(\overrightarrow{\lambda}, z|0) = \underline{I}_t \frac{\cosh(pd)}{p \sinh(pd)} \tag{2.26}$$

with

$$p = \sqrt{\xi^2 + \eta^2 - k^2}. \tag{2.27}$$

After transforming the Green's function, rearranging the order of integration, and pulling out constants, equations 2.22 and 2.23 become

$$\begin{aligned} \frac{1}{j\omega\mu(2\pi)^2} \iint_{-\infty}^{\infty} \iint_{S_1} e^{j\xi x} e^{j\eta y} \Bigg[ \iint_{S_1} e^{-j\xi x'} e^{-j\eta y'} \left( (k^2 \underline{I}_t + \nabla_t \nabla \cdot) \widetilde{\underline{G}}(\overrightarrow{\lambda}, z|0) \cdot \left( -\hat{n} \times \overrightarrow{E}^1_{tDRWG} \right) \right) \\ + \iint_{S_2} e^{-j\xi x'} e^{-j\eta y'} \left( (k^2 \underline{I}_t + \nabla_t \nabla \cdot) \widetilde{\underline{G}}(\overrightarrow{\lambda}, z|0) \cdot \left( -\hat{n} \times \overrightarrow{E}^2_{tDRWG} \right) \right) \Bigg] \\ \cdot \overrightarrow{h}_t^{1*} \, ds' \, ds \, d\eta \, d\xi \\ = \iint_{S_1} \left( (1 - \Gamma) \overrightarrow{h}_t^1(\overrightarrow{\rho}) \right) \cdot \overrightarrow{h}_t^{1*} \, dS_1. \end{aligned} \tag{2.28}$$

$$\frac{1}{j\omega\mu(2\pi)^2}\iint_{-\infty}^{\infty}\iint_{S_2} e^{j\xi x}\, e^{j\eta y}\Bigg[\iint_{S_1} e^{-j\xi x'}\, e^{-j\eta y'}\left((k^2\underline{I}_t+\nabla_t\nabla\cdot)\,\underline{\widetilde{G}}(\overrightarrow{\lambda},z|0)\cdot\left(-\hat{n}\times\overrightarrow{E}^1_{tDRWG}\right)\right)$$
$$+\iint_{S_2} e^{-j\xi x'}\, e^{-j\eta y'}\left((k^2\underline{I}_t+\nabla_t\nabla\cdot)\,\underline{\widetilde{G}}(\overrightarrow{\lambda},z|0)\cdot\left(-\hat{n}\times\overrightarrow{E}^2_{tDRWG}\right)\right)\Bigg]$$
$$\cdot\,\overrightarrow{h}^{2*}_t\, ds'\, ds\, d\eta\, d\xi$$
$$=-\iint_{S_2}\left(\mathrm{T}\overrightarrow{h}^2_t(\overrightarrow{\rho})\right)\cdot\overrightarrow{h}^{2*}_t dS_2 \tag{2.29}$$

Once all operations are conducted on 2.28 and 2.29, a series of six dimensional integrals remain on the left of the equalities, and a double integral remains on the right of the equalities. The double integral to the right has three sections that must be calculated separately, one for each subregion of the waveguide. These integrals are straightforward and easily calculated using standard trigonometric identities and integration of trigonometric functions. The left side integrals are more complicated. In the dual probe system 64 total 6 dimensional integrals must be calculated. One example of these 6 dimensional integrals is shown below

$$\sum_{n,m}\sum_{\tilde{n},\tilde{m}} e^t_{yn,m}\, e^{t*}_{y\tilde{n},\tilde{m}}\int_{-\infty}^{\infty}\left(k^2-\xi^2\right) f_{m,\tilde{m}}(\xi)\int_{-\infty}^{\infty}\frac{\cosh(pd)}{p\,\sinh(pd)} g_{m,\tilde{m}}(\eta)\, d\eta\, d\xi \tag{2.30}$$

where

$$f_{m,\tilde{m}}(\xi)=\int_{\Delta x}^{\frac{a}{2}}\sin\left[k^t_{xm}\left(\frac{a}{2}-x'\right)\right]\cos(\xi x')\; dx'\int_{\Delta x}^{\frac{a}{2}}\sin\left[k^t_{x\tilde{m}}\left(\frac{a}{2}-x\right)\right]\cos(\xi x)\; dx \tag{2.31}$$

and

$$g_{m,\tilde{m}}(\eta)=\int_{-\frac{b}{2}}^{\frac{b}{2}} cos\left[k^t_{ym}\left(y'-\frac{b}{2}\right)\right] e^{-j\eta y'}\, dy'\int_{-\frac{b}{2}}^{\frac{b}{2}} cos\left[k^t_{y\tilde{m}}\left(y-\frac{b}{2}\right)\right] e^{-j\eta y}\, dy. \tag{2.32}$$

In these integrals the integration over spacial variables is easily computed using trigonometric identities and integration of trigonometric functions. However, integrals over spectral variables $(\xi,\eta)$ are more complicated. The integral over $\eta$ can be computed

relatively easily using complex plane analysis. This process for the example in expression 2.30 is shown in the next section.

## 2.5 Integrating $\eta$ Using Complex Plane Analysis

In order to evaluate the $\eta$ integral in expression 2.30, complex plane analysis is used. Once $g_{m,\tilde{m}}(\eta)$ has been evaluated and substituted into 2.30 the $\eta$ integral has the form

$$\int_{-\infty}^{\infty} \frac{\cosh(pd)}{p\sinh(pd)}\eta^2 \frac{1-(-1)^{\tilde{m}}e^{-j\eta 2\Delta y}}{\left(\eta^2-\left(\frac{m\pi}{b}\right)\right)\left(\eta^2-\left(\frac{\tilde{m}\pi}{b}\right)\right)}d\eta$$
$$+(-1)^m\int_{-\infty}^{\infty} \frac{\cosh(pd)}{p\sinh(pd)}\eta^2 \frac{(-1)^{\tilde{m}}-e^{j\eta 2\Delta y}}{\left(\eta^2-\left(\frac{m\pi}{b}\right)\right)\left(\eta^2-\left(\frac{\tilde{m}\pi}{b}\right)\right)}d\eta \tag{2.33}$$

In order to evaluate expression 2.33 it is first broken up into 5 cases. These cases involve differing values of $m$ and $\tilde{m}$. As these values change, pole locations for the function will change, and alter the outcome of the integral. The order of the poles will also change as $m$ and $\tilde{m}$ vary. Pole plots for these cases is shown in Figure 2.5. Note that $dp$ next to a pole indicates a double pole.

Setting the denominator of 2.33 equal to 0 identifies all singularities. Poles $\eta_p^+$ and $\eta_p^-$ arise from the parallel plate structure due to the Green's function term $\sinh(pd) = 0$. Note that because of the cyclical nature of the sinh function, in actuality there are an infinite number of these poles. However, only one is shown in the pole plot for simplicity. Examination of the denominator of 2.33 also reveals there is a double pole at $\eta_p^0 = 0$ for the case of $m = \tilde{m} = 0$ (however it will be shown that one of these poles is removable). In addition there are either single or double poles located at $\eta_1^+ = \frac{m\pi}{b}$, $\eta_1^- = -\frac{m\pi}{b}$, $\eta_2^+ = \frac{\tilde{m}\pi}{b}$, and $\eta_2^- = -\frac{\tilde{m}\pi}{b}$ depending on the values of $m$ and $\tilde{m}$. There is a branch point and associated branch cut resulting from $p = 0$ where $p$ is defined in equation 2.27, but due to the evenness of the function in $p$, it is removable and therefore does not contribute. Here, details for the evaluation of 2.33 using complex plane analysis is shown for the case $m = \tilde{m} = 0$. Other

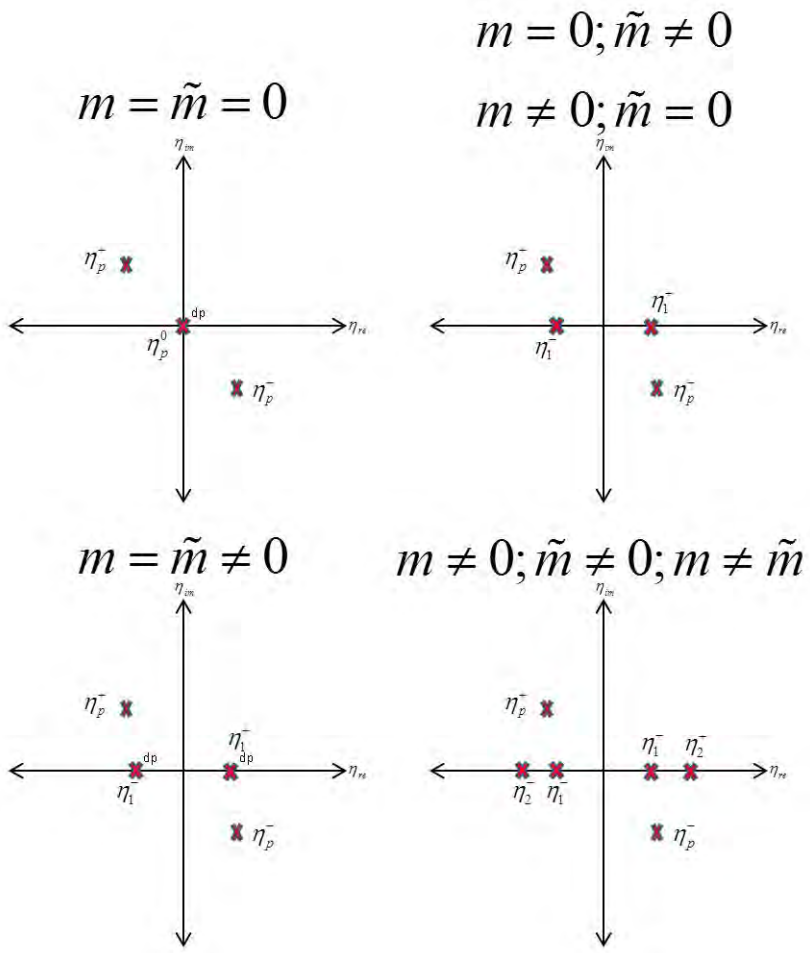


Figure 2.5: Pole locations for 5 cases considered in the complex plane analysis.

cases are omitted for brevity but can be treated in a similar manner. If $m$ and $\tilde{m}$ are set to 0, expression 2.33 becomes

$$\int_{-\infty}^{\infty} \frac{\cosh(pd)}{p\sinh(pd)} \frac{1 - e^{-j\eta 2\Delta y}}{\eta^2} d\eta + \int_{-\infty}^{\infty} \frac{\cosh(pd)}{p\sinh(pd)} \frac{1 - e^{j\eta 2\Delta y}}{\eta^2} d\eta \tag{2.34}$$

Here we examine the second integral portion of 2.34. Cauchy's Integral Theorem states that

$$\oint_C f(z)\,dz \;=\; 0 \tag{2.35}$$

for a simple closed contour as long as the function $f(z)$ is analytic inside and on the contour. Thus we are allowed to define a contour around the poles in figure 2.5. Closure in the upper half plane ensures that the conditions of Jordan's Lemma [1] are satisfied. This contour is shown in Figure 2.6.

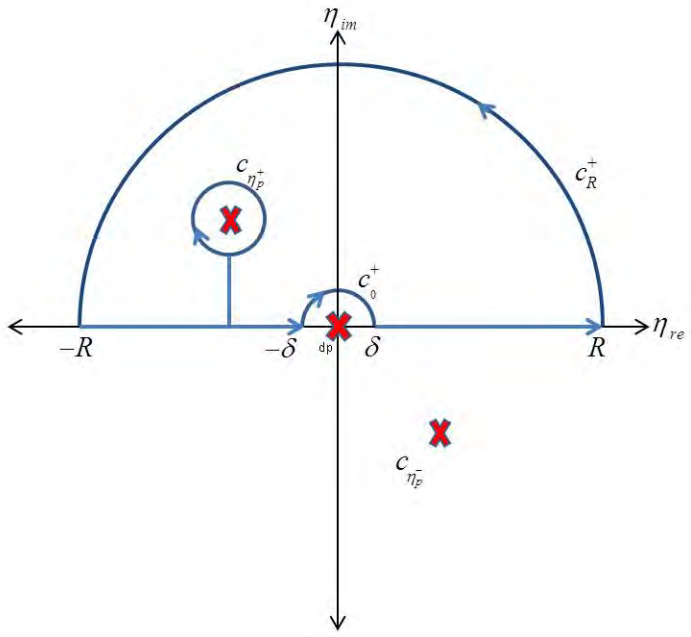


Figure 2.6: Contour for upper half plane closure where $m$ and $\tilde{m}$ equal 0.

Choosing this contour allows us to use Cauchy's Integral Theorem such that

$$\oint_C f(z)\,dz \;=\; \int_{-R}^{-\delta} + \int_{\delta}^{R} + \sum_{\ell=0}^{\ell_R} \oint_{C_{\eta_{p_\ell}^+}} + \int_{c_0^+} + \int_{c_R^+} \;=\; 0. \tag{2.36}$$

Using Cauchy's Integral Formula for single poles, the parallel-plate mode contribution from the third term on the right hand side of 2.36 becomes

$$\frac{j2\pi}{d} \sum_{\ell=0}^{\ell_R} \frac{1 - e^{-j\eta_\ell 2\Delta y}}{\eta_\ell^3 (1 + \delta_{\ell,0})}. \tag{2.37}$$

Since the pole at the origin is a double pole, Cauchy's Integral Formula for higher order poles is used namely,

$$\oint_C \frac{f(\eta)}{(\eta-\eta_0)^n}\,d\eta \;=\; \frac{j\pi}{(n-1)!}\frac{d^{n-1}f(\eta)}{d\eta^{n-1}}\bigg|_{\eta=\eta_0} \tag{2.38}$$

for a half circle where $n$ is the order of the pole. In this problem

$$f(\eta) = \frac{\cosh(pd)}{p\sinh(pd)}\left(1-e^{j\eta 2\Delta y}\right) \tag{2.39}$$

and $n = 2$. Using 2.38 on 2.39 yields

$$j\pi\left[\frac{\cosh(pd)}{p\sinh(pd)}\left(-j2\Delta y e^{j\eta 2\Delta y}\right)\bigg|_{\eta=0} + \left(1-e^{j\eta 2\Delta y}\right)\frac{d}{d\eta}\frac{\cosh(pd)}{p\sinh(pd)}\bigg|_{\eta=0}\right] \tag{2.40}$$

It is easy to see that the second half of expression 2.40 goes to 0 when it is evaluated at $\eta = \eta_0 = 0$. Thus the contribution from $C_0^+$ becomes

$$2\pi\Delta y\frac{\cosh(p_0 d)}{p_0\sinh(p_0 d)} \tag{2.41}$$

where $p_0 = \sqrt{\xi^2-k^2}$. It is also easily shown using the substitution $\eta = Re^{j\theta}$ that the integrand from $C_R^+$ adheres to Jordan's Lemma and therefore has 0 contribution as $R \to \infty$. Finally using Cauchy's Integral Theorem in the limit as $R$ approaches $\infty$ and $\delta$ approaches $0^+$, it can be shown that

$$\lim_{\delta\to 0^+}\lim_{R\to\infty}\left(\int_{-R}^{-\delta} + \int_{\delta}^{R}\right) = PV\int_{-\infty}^{\infty} = 2\pi\Delta y\frac{\cosh(p_0 d)}{p_0\sinh(p_0 d)} - \frac{j2\pi}{d}\sum_{\ell=0}^{\infty}\frac{1-e^{-j\eta_\ell 2\Delta y}}{\eta_l^3(1+\delta_{n,0})} \tag{2.42}$$

where $PV$ denotes the integral has been computed in a principle value sense. Note that as $R$ approaches $\infty$ more parallel plate poles are included. The first half of 2.34 uses the same process as the second half. However, note that this portion must be closed in the lower half plane to ensure satisfaction of Jordan's Lemma. A contour for lower half closure is shown in Figure 2.7

After using the process detailed above it can be shown that the first half of 2.34 evaluates to the same expression as the second half of 2.34. Thus the final form of 2.34 is

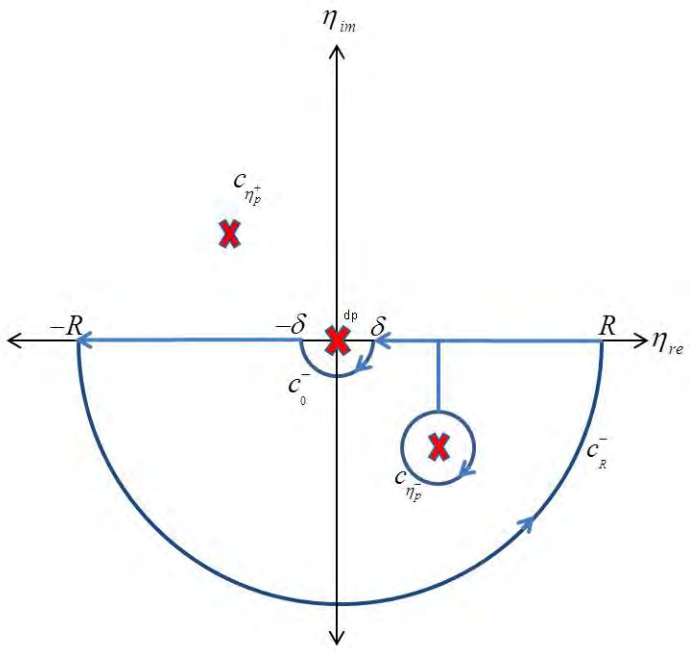


Figure 2.7: Contour for lower half plane closure where $m$ and $\tilde{m}$ equal 0.

simply twice the value of equation 2.42. Once this case is complete, the 4 other cases for this example are evaluated using the same steps. The 63 other integrals are also evaluated using the same steps.

## 2.6 Calculating $\Gamma$ and T

Once all $\eta$ integrals are evaluated, the $\xi$ integrals are computed numerically. These integrals contain branch cuts and cannot be found in closed form. MATLAB was used for all code and simulations for this research. Gaussian quadrature was used to integrate all $\xi$ integrals. Once all $\xi$ integrals are calculated a linear system of equations remains where $\Gamma$ and T are the unknowns. This system can be rearranged such that:

$$\begin{bmatrix} a_{1,1} & a_{1,2} \\ a_{2,1} & a_{2,2} \end{bmatrix} \begin{bmatrix} \Gamma \\ \mathrm{T} \end{bmatrix} = \begin{bmatrix} b_1 \\ b_2 \end{bmatrix}. \tag{2.43}$$

## 2.7 Simulated Dual Probe DRWG Results

Results for simulating the dual probe DRWG system are shown below. Fixed parameters of the system are shown in Table (2.1). The MUT for this simulation was FGM125, a thin, flexible, broadband, magnetically loaded silicone absorber [28].

Table 2.1: Simulation parameters for the dual probe DRWG system showing dimensions for the DRWGs and fgm125 parameters.

| | |
|---|---|
| $a$ | .0183 m |
| $b$ | .0082 m |
| $\Delta x$ | .0022 m |
| $\Delta y$ | .0013 m |
| $y_0$ | (1.01 $\times$ b) m |
| $d$ | .0031 m |
| $MUT$ | fgm125 |
| $\epsilon_r$ | 6.7314 - 0.2225i |
| $\mu_r$ | 0.6202 - 0.2960i |
| $f$ | 6.0 GHz |

Initial simulation results were used to confirm the MATLAB code is working. A result for $\Gamma$ and $T$ was obtained and was physically realizable. It was expected that the magnitude of both reflection and transmission coefficients would range somewhere between 0 and 1. After the initial test concluded, another series of simulations were conducted to further test the system. The first of these tests consisted of varying $y_0$. Because of the lossy material simulated, the expectation is that by increasing $y_0$, $T$ should decrease; and by decreasing $y_0$, $T$ should increase. These results are shown in table (2.2). The second test consisted of varying $\mu_r$. The expectation is that by decreasing the imaginary component of $\mu_r$ (making

the material low loss) $T$ will increase because less energy is lost in the MUT. These results are shown in table (2.3).

Table 2.2: Results of Varying $y_0$ showing decreases in T as $y_0$ increases for lossy media

| $y_0$ | $\|T\|$ |
|---|---|
| $1.0001 \times b$ | .0502 |
| $1.01 \times b$ | .0499 |
| $1.5 \times b$ | .0367 |
| $10 \times b$ | $1.9\ e^{-4}$ |

Table 2.3: Results of Varying $\mu_r$ showing increases in T as $\mu_r$ decreases for lossy media

| $\mu_r$ | $\|T\|$ |
|---|---|
| $0.6202 - 0.2960i$ | .0499 |
| $0.6202 - 0.1i$ | .0659 |
| $0.6202 - 0.01i$ | .0779 |

Tables 2.2 and 2.3 show all results are trending as expected. It also shows that, while using lossy media, T decreases to essentially 0 if the probes are placed too far apart. This implies that when using lossy media the two DRWG probes need to be as close as possible to ensure sufficient coupling to obtain an accurate T measurement. A further simulation was conducted to determine if the minimum physical distance between waveguides is sufficient to measure T in lossy media. In this simulation the same lossy MUT was used at a frequency of 12 GHz. Waveguide offset $y_0$ was then varied in finer increments. These results are shown in Figure (2.8).

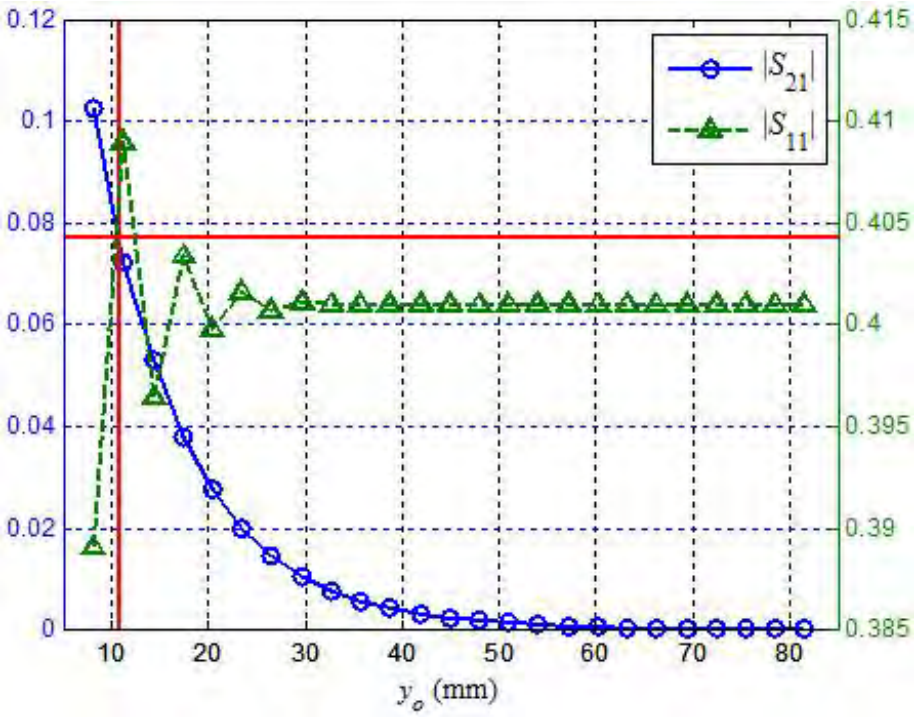


Figure 2.8: Γ and T versus $y_0$ showing the minimum distance between waveguides for lossy material

These simulation results confirm that the minimum realizable $y_0$ distance denoted by the red lines will ensure a measurable transmission coefficient for lossy media. It also shows oscillating behavior in the reflection measurement. This can be attributed to coupling between the two waveguides going in and out of phase. A final simulation was conducted to determine how the system would behave when a low loss material was used instead of a high loss material. The low loss material simulated was Teflon with material parameters $\epsilon_r = 2.1 - j.001$ and $\mu_r = 1$. The simulation used the same waveguide parameters at a frequency of 12 GHz. Results of this simulation are shown in Figure 2.9.

Figure 2.9 shows that, as expected, T does not decrease as fast for low loss material. This allows for greater spacing between waveguides when taking low loss measurements. It may also be beneficial to have the probes farther apart to allow the waves to interact further

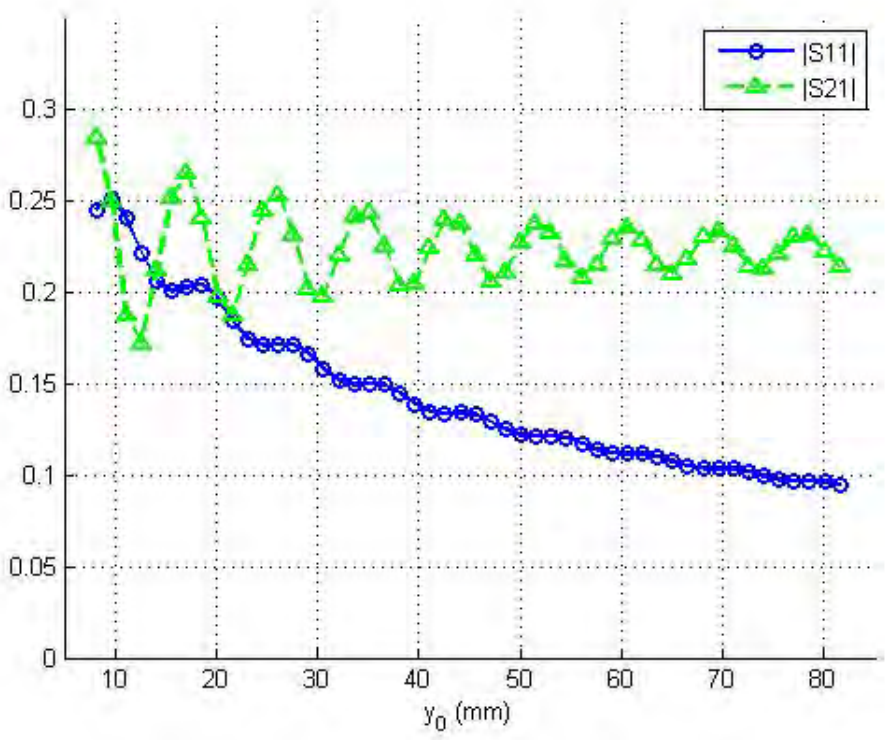


Figure 2.9: Γ and T versus $y_0$ for low loss material.

in distance with the low loss material. Again oscillation is seen in the measurements, a further sign of constructive and destructive interference coupling between the waveguides. Because of this oscillation, it makes determining the best spacing between probes more difficult for low loss material. It is recommended that the probes be spaced in such a way that the measurement occurs on the flatter part of the curves. This will help reduce measurement errors associated with errors in $y_0$. However, the flatter part of the curve will move as the frequency changes. This may render choosing the spacing based on minimization of errors due to $y_0$ more difficult.

Comparing Figures 2.8 and 2.9, both show exponential decay in the transmission measurement. Differences in decay rate are driven by the amount of loss and wave spreading in each material. However, in the event of a lossless material, there would still

be algebraic decay based on wave spreading. Upon consideration of the findings in Figures 2.8 and 2.9, it is concluded that sufficient coupling does occur for both lossy and lowloss materials. Thus, the dual probe DRWG comprises a valuable candidate as a flight-line diagnostic tool.

# III. Multimode Single Probe DRWG

In this chapter, the analysis of a single probe DRWG, shown in Figure (3.1), is performed. The analysis includes an examination of the reflection coefficients of the dual probe DRWG placed on a conductor-backed material. It is assumed in the analysis that only a single dominant mode is propagating in the free-space filled DRWG however, higher order evanescent modes are allowed to exist during the analysis. The fundamental goal for performing this analysis is to assess if a single mode is sufficient to accurately determine permittivity and permeability of the material, or whether higher order modes must be included in the analysis to obtain accurate permittivity and permeability results. This answer will greatly impact the ability to perform these measurements in real time, versus needing a large amount of time and resources to post-process.

The multimode single probe DRWG analysis uses the same field expressions detailed in chapter 2. First field expressions in the DRWG are defined. Next, the fields in the PP region of the single probe DRWG are found with the aid of Love's Equivalence Theorem. Subsequent enforcement of tangential boundary conditions at the single probe DRWG aperture leads to a MFIE for the unknown reflection coefficient. Recall however, that if two material properties are desired, two linearly-independent measurements are required. To obtain this second independent measurement, a two thickness technique is used where another reflection measurement is taken for the same material of a different thickness. The two coupled MFIE's are solved via the Method-of-Moments for a lossy material. Experimental results for the calculation of $\epsilon_r$ and $\mu_r$ are presented and discussed, and general conclusions are provided.

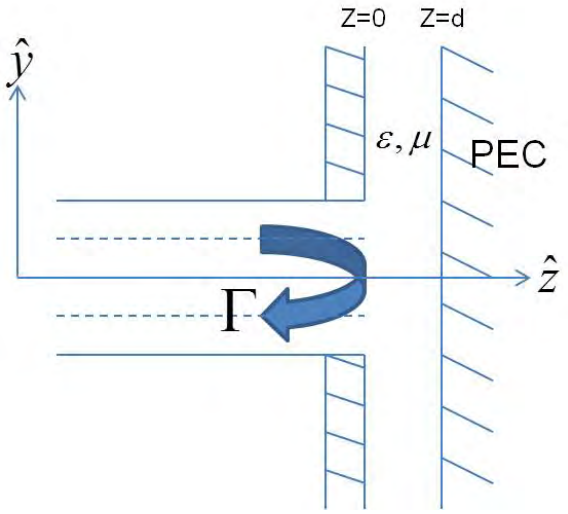


Figure 3.1: Side view of single probe DRWG geometry

## 3.1 Single Probe DRWG Region Fields

As a wave travels down the DRWG and interacts with the boundary between the waveguide and the MUT, a portion of the energy will be reflected back into the waveguide [5]. Thus we must first find the total fields in the DRWG region. All fields in a single probe DRWG system are found using a process similar to that used in chapter 2. Total fields in the DRWG portion of the system are found using the DRWG fields developed in chapter 2. While chapter 2 only uses a single propagating mode, a more robust multi-mode analysis allows for multiple reflection coefficients for many potential waveguide modes. Allowing for this yields fields in the form of

$$\overrightarrow{E}_{DRWG} = e^{-jk_z z}\overrightarrow{e}_{t1}(\overrightarrow{\rho}) + \sum_{q=1}^{N} \Gamma_q e^{jk_z z}\overrightarrow{e}_{tq}(\overrightarrow{\rho}) \tag{3.1}$$

$$\overrightarrow{H}_{DRWG} = e^{-jk_z z}\overrightarrow{h}_{t1}(\overrightarrow{\rho}) - \sum_{q=1}^{N} \Gamma_q e^{jk_z z}\overrightarrow{h}_{tq}(\overrightarrow{\rho}) \tag{3.2}$$

where

$$\overrightarrow{e}_t = \hat{x}E_x + \hat{y}E_y \tag{3.3}$$

$$\overrightarrow{h}_t = \frac{\hat{z} \times \overrightarrow{e}_t}{Z^{TE}}. \tag{3.4}$$

Variable $\Gamma_q$ is the reflection coefficient associated with the $q^{th}$ even mode. Only even modes are considered because the dominant mode is even symmetric and the system is even symmetric. This forces all possible excited modes to be even. Variable $N$ is the number of modes allowed to be reflected and can be as small or large as required for convergence. Upon inspection it is easy to see that equations 3.1 and 3.2 simplify to an equation similar to that of 2.6 and 2.7 if $N = 1$ and only one reflected mode is considered.

### 3.2 Parallel Plate Region Fields

As a wave travels down the DRWG and contacts the interface between the waveguide and the MUT, a portion of the energy will be transmitted into the MUT. This energy gives rise to electromagnetic fields inside the PP region of the system. These fields are found using a process similar to that used in chapter 2. First Love's equivalence principle [5] is used to replace the actual source (the DRWG aperture) with an equivalent source in the form of magnetic surface currents, namely [5]

$$\overrightarrow{M} = -\hat{n} \times \overrightarrow{E}. \tag{3.5}$$

where $\hat{n}$ the normal unit vector points into the MUT region. This equivalent system is shown in Figure (4.2).

Now that the equivalent current has been identified, a vector potential (VP) solution is used to find the parallel plate region fields. This solution is as follows:

$$\overrightarrow{H}_t^{pp}(\overrightarrow{\rho}, z) = \frac{1}{j\omega\epsilon\mu}(k^2 \underline{I}_t + \nabla_t \nabla \cdot)\overrightarrow{F}_t^{pp}(\overrightarrow{\rho}, z). \tag{3.6}$$

However, the $\overrightarrow{F}$ VP must first be identified. The surface current $\overrightarrow{M}_1$ supports this vector through the following relation,

$$\overrightarrow{F}_t^{pp}(\overrightarrow{\rho}, z) = \iint_{S_1} \underline{G}(\overrightarrow{\rho}, z|\overrightarrow{\rho}', 0) \cdot \epsilon \overrightarrow{M}_1(\overrightarrow{\rho}')ds' \tag{3.7}$$

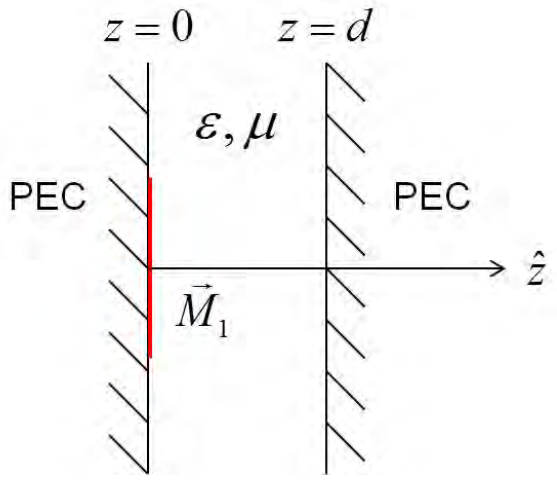


Figure 3.2: Equivalent system for parallel plate region of the single probe DRWG system after Love's Equivalence Theorem is applied.

where $\underline{G}(\vec{\rho}, z|\vec{\rho}', 0)$ is the parallel plate Green's function, and $\vec{M}_1$ is found using equation 3.5. Equating the tangential magnetic field at the aperture leads to the MFIE

$$\frac{1}{j\omega\epsilon\mu}(k^2\underline{I}_t + \nabla_t\nabla\cdot)\vec{F}_t^{pp}(\vec{\rho}, z) = \vec{h}_{t1}(\vec{\rho}) - \sum_{q=1}^{N}\Gamma_q\vec{h}_{tq}(\vec{\rho}). \tag{3.8}$$

This MFIE is solved in the next section via the MoM.

### 3.3 Solving the MFIE

This section details solving the MFIE of the previous section. The first step of the MoM is to expand the unknown current ($\vec{M}_1$) as a series of basis functions. In this case we will exploit the fact that we know the fields in the DRWG region just to the left of the boundary, and we know that these fields must be continuous across the boundary, namely

$$\vec{M}_1(\vec{\rho}') = -\hat{n}\times\vec{E} \approx -\hat{n}\times\vec{E}_{DRWG}. \tag{3.9}$$

Substituting 3.9 into 3.7 and further substituting into 3.8 yields the following relation after expansion:

$$\frac{1}{j\omega\mu}(k^2\underline{I}_t + \nabla_t\nabla\cdot)\iint_{S_1}\underline{G}(\overrightarrow{\rho},z|\overrightarrow{\rho}',0)\cdot\left(-\hat{n}\times\overrightarrow{E}_{DRWG}\right)ds' = \overrightarrow{h}_{t1}(\overrightarrow{\rho}) - \sum_{q=1}^{N}\Gamma_q\overrightarrow{h}_{tq}(\overrightarrow{\rho}) \quad (3.10)$$

Next both sides of equation 3.10 are tested with $N$ total magnetic field modes. This must be done $N$ times because there are $N$ unknowns in the form of $\Gamma_1$ through $\Gamma_N$. The testing operator is as follows:

$$\iint_{S_1}\{\cdots\}\cdot\overrightarrow{h}^*_{t\tilde{q}}dS_1 \quad (3.11)$$

After testing, 3.10 becomes

$$\begin{aligned}\iint_{S_1}\left(\frac{1}{j\omega\mu}(k^2\underline{I}_t + \nabla_t\nabla\cdot)\iint_{S_1}\underline{G}(\overrightarrow{\rho},z|\overrightarrow{\rho}',0)\cdot\left(-\hat{n}\times\overrightarrow{E}_{DRWG}\right)ds'\right)\cdot\overrightarrow{h}^*_{t\tilde{q}}dS_1 \\ = \iint_{S_1}\left(\overrightarrow{h}_{t1} - \sum_{q=1}^{N}\Gamma\overrightarrow{h}_{tq}(\overrightarrow{\rho})\right)\cdot\overrightarrow{h}^*_{t\tilde{q}}dS_1.\end{aligned} \quad (3.12)$$

From this point forward it is desirable to work with the spectral representation of the Green's function. The Green's function is shown below

$$\underline{G}(\overrightarrow{\rho},z|\overrightarrow{\rho}',0) = \frac{1}{(2\pi)^2}\iint_{-\infty}^{\infty}\widetilde{\underline{G}}(\overrightarrow{\lambda},z|0)e^{j\xi(x-x'_1)}e^{j\eta(y-y'_1)}d\xi d\eta \quad (3.13)$$

where

$$\widetilde{\underline{G}}(\overrightarrow{\lambda},z|0) = \underline{I}_t\frac{\cosh(pd)}{p\sinh(pd)} \quad (3.14)$$

and

$$p = \sqrt{\xi^2+\eta^2-k^2}. \quad (3.15)$$

After using this Green's function, rearranging the order of integration, and pulling out constants, equation 3.12 becomes

$$\begin{aligned}\frac{1}{j\omega\mu(2\pi)^2}\iint_{-\infty}^{\infty}\iint_{S_1}e^{j\xi x}\,e^{j\eta y}\iint_{S_1}e^{-j\xi x'}\,e^{-j\eta y'} \\ \left((k^2\underline{I}_t + \nabla_t\nabla\cdot)\,\widetilde{\underline{G}}(\overrightarrow{\lambda},z|0)\cdot\left(-\hat{n}\times\overrightarrow{E}_{DRWG}\right)\right)\cdot\overrightarrow{h}^*_{t\tilde{q}}\,ds'\,ds\,d\eta\,d\xi \\ = \iint_{S_1}\left(\overrightarrow{h}_{t1} - \sum_{q=1}^{N}\Gamma\overrightarrow{h}_{tq}(\overrightarrow{\rho})\right)\cdot\overrightarrow{h}^*_{t\tilde{q}}\,dS_1.\end{aligned} \quad (3.16)$$

Once all operations are conducted on 3.16, a series of six dimensional integrals remain on the left of the equality, and a double integral remains on the right of the equality. The double integral on the right has three sections that must be calculated separately, one for each region of the waveguide. These integrals are straightforward and easily calculated using standard trigonometric identities and integration of trigonometric functions. Note these integrals must be calculated $N$ times due to there being $N$ unknowns. Because the waveguide modes are orthogonal only values where expansion and testing indices are equal ($q = \tilde{q}$) need to be calculated. The following expression is the final solution to the right side double integral of equation 3.16 where $q = \tilde{q} = 1$.

$$\begin{aligned}
\frac{1-\Gamma_1}{|Z^{TE}|^2}\Bigg[ & \sum_n |e^g_{yn}|^2 4\alpha_n^2 \left(\mathrm{sinc}(2jk^g_{xn,im}\Delta x) + \mathrm{sinc}(2k^g_{xn,re}\Delta x)\right)\Delta x\Delta y(1+\delta_{n,0}) \\
& + \sum_n |e^g_{xn}|^2 4\alpha_n^2 \left(\mathrm{sinc}(2jk^g_{xn,im}\Delta x) - \mathrm{sinc}(2k^g_{xn,re}\Delta x)\right)\Delta x\Delta y(1-\delta_{n,0}) \\
& + \sum_{\tilde{n}}\sum_{n,m} \alpha_n\alpha^*_{\tilde{n}} e^t_{ymn} e^{t*}_{ym\tilde{n}} \Bigg(\mathrm{sinc}\left(2jk^t_{xm,im}\left(\frac{a}{2}-\Delta x\right)\right) \\
& -\mathrm{sinc}\left(2k^t_{xm,re}\left(\frac{a}{2}-\Delta x\right)\right)\Bigg)\left(\frac{a}{2}-\Delta x\right)\frac{b}{2}(1+\delta_{m,0}) \\
& + \sum_{\tilde{n}}\sum_{n,m} \alpha_n\alpha^*_{\tilde{n}} e^t_{xmn} e^{t*}_{xm\tilde{n}} \Bigg(\mathrm{sinc}\left(2jk^t_{xm,im}\left(\frac{a}{2}-\Delta x\right)\right) \\
& +\mathrm{sinc}\left(2k^t_{xm,re}\left(\frac{a}{2}-\Delta x\right)\right)\Bigg)\left(\frac{a}{2}-\Delta x\right)\frac{b}{2}(1-\delta_{m,0})\Bigg]
\end{aligned} \tag{3.17}$$

The left side integrals are more complicated. In the single probe system 16 total 6 dimensional integrals must be calculated for each combination of $q$ and $\tilde{q}$ leading to a total of $N^2\times 16$ six dimensional integrals. One example of these 6 dimensional integrals is shown below

$$\sum_{n,m}\sum_{\tilde{n},\tilde{m}} e^t_{yn,m}\, e^{t*}_{y\tilde{n},\tilde{m}} \int_{-\infty}^{\infty}\left(k^2-\xi^2\right) f_{m,\tilde{m}}(\xi)\int_{-\infty}^{\infty}\frac{\cosh(pd)}{p\ \sinh(pd)} g_{m,\tilde{m}}(\eta)\, d\eta\, d\xi \tag{3.18}$$

where

$$f_{m,\tilde{m}}(\xi) = \int_{\Delta x}^{\frac{a}{2}} \sin\left[k_{xm}^{t}\left(\frac{a}{2} - x'\right)\right] \cos(\xi x')\ dx' \int_{\Delta x}^{\frac{a}{2}} \sin\left[k_{x\tilde{m}}^{t}\left(\frac{a}{2} - x\right)\right] \cos(\xi x)\ dx \quad (3.19)$$

and

$$g_{m,\tilde{m}}(\eta) = \int_{-\frac{b}{2}}^{\frac{b}{2}} cos\left[k_{ym}^{t}\left(y' - \frac{b}{2}\right)\right] e^{-j\eta y'}\ dy' \int_{-\frac{b}{2}}^{\frac{b}{2}} cos\left[k_{y\tilde{m}}^{t}\left(y - \frac{b}{2}\right)\right] e^{-j\eta y}\ dy. \quad (3.20)$$

In this example integrals with respect to spatial variables $(x, x', y, y')$ are easily computed using trigonometric identities and integration of trigonometric functions. However, integrals over spectral variables $(\xi, \eta)$ are more complicated. The integral over $\eta$ can be computed relatively easily using complex plane analysis i.e. Cauchy's theorem. For more information on complex plane integration see chapter 2. Once all $\eta$ integrals are computed the $\xi$ integrals are computed numerically. These integrals contain branch cuts and cannot be found in closed form. MATLAB was used for all code and simulations for this research. Gaussian quadrature was used to integrate all $\xi$ integrals. Once all $\xi$ integrals are calculated a linear system of equations remains where $\Gamma_1$ through $\Gamma_N$ are the unknowns. This system can be rearranged such that:

$$\begin{bmatrix} a_{11} & \cdots & a_{1q} & \cdots & a_{1N} \\ \vdots & \ddots & & & \vdots \\ a_{\tilde{q}1} & & a_{\tilde{q}q} & & a_{\tilde{q}N} \\ \vdots & & & \ddots & \vdots \\ a_{N1} & \cdots & a_{Nq} & \cdots & a_{NN} \end{bmatrix} \begin{bmatrix} \Gamma_1 \\ \vdots \\ \Gamma_{\tilde{q}} \\ \vdots \\ \Gamma_N \end{bmatrix} = \begin{bmatrix} b_1 \\ \vdots \\ b_{\tilde{q}} \\ \vdots \\ b_N \end{bmatrix}. \quad (3.21)$$

It is important to note that although there are multiple unknowns in equation 3.21, these values are not typically measurable. Only $\Gamma_1$ is typically measured since it represents reflection of the dominant propagating mode. In order to get a second independent measurement and solve for both permittivity and permeability, a two thickness technique is used to get the second measurement. This second measurement uses the exact same process as previously described where the only difference is the thickness of the MUT. Because the

derivation is exactly the same, no new theoretical calculations need to be done. The exact same MATLAB code used to determine equation 3.21 is used with a second thickness. This second thickness for this research is simply double the original thickness. To take experimental measurements, two layers of MUT are used instead of one. This second linear system of equations is arranged such that:

$$\begin{bmatrix} a_{11}^2 & \cdots & a_{1q}^2 & \cdots & a_{1N}^2 \\ \vdots & \ddots & & & \vdots \\ a_{\tilde{q}1}^2 & & a_{\tilde{q}q}^2 & & a_{\tilde{q}N}^2 \\ \vdots & & & \ddots & \vdots \\ a_{N1}^2 & \cdots & a_{Nq}^2 & \cdots & a_{NN}^2 \end{bmatrix} \begin{bmatrix} \Gamma_1^2 \\ \vdots \\ \Gamma_{\tilde{q}}^2 \\ \vdots \\ \Gamma_N^2 \end{bmatrix} = \begin{bmatrix} b_1^2 \\ \vdots \\ b_{\tilde{q}}^2 \\ \vdots \\ b_N^2 \end{bmatrix}. \tag{3.22}$$

where superscript 2 denote computations for thickness 2. Once equations 3.21 and 3.22 is complete material parameters $\epsilon$ and $\mu$ can be calculated.

### 3.4 Calculating $\epsilon$ and $\mu$

Now that all calculations needed to obtain and solve equations 3.21 and 3.22 are complete, material parameters $\epsilon$ and $\mu$ can be computed. In this step these parameters are solved iteratively using a least squares technique. First an initial guess for $\epsilon$ and $\mu$ is used to calculate initial $\Gamma_1^1$ and $\Gamma_1^2$ estimates. These estimates are compared to experimental measurements taken from a single probe system. Experimental measurement data used was the same data obtained and used in [21]. After comparing $\Gamma_1^1$ and $\Gamma_1^2$ to reflection coefficients of the experimental system, an update to $\epsilon$ and $\mu$ is calculated and used to recalculate $\Gamma_1^1$ and $\Gamma_1^2$. This process happens repeatedly until the difference in $\Gamma_1^1$ and $\Gamma_1^2$ and the experimental data is within tolerances set by the user. MATLAB's lsqcurvefit function was used to perform the iterative least squares operation. Experimental results of this process are shown in the next section.

### 3.5 ECCOSORB SF-3 Experimental Results

This section details the experimental results using multiple modes for the single probe DRWG system. All experimental data came from [21], see this for more details on the experimental setup and equipment used. In this experiment, material characterization measurements were made at 6-18 GHz of a lossy silicon-based magnetic absorbing material ECCOSORB SF-3 [16] manufactured by Emerson & Cuming Microwave Products, Inc. Figures (3.3) and (3.4) show calculated $\epsilon$ and $\mu$ values respectively. Both figures show calculations for 1 through 3 modes, and also experimental results using a Nicholson-Ross-Weir (NRW) method [22].

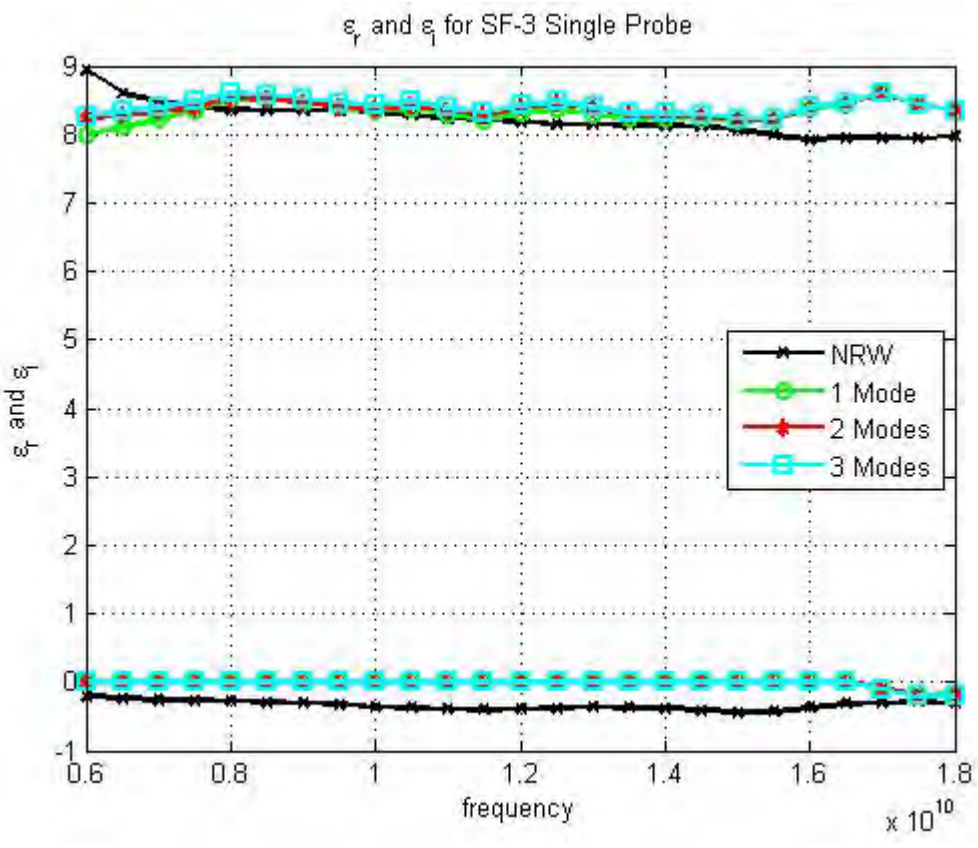


Figure 3.3: Calculated $\epsilon$ values for 1 - 3 modes as well as experimental results using a NRW method.

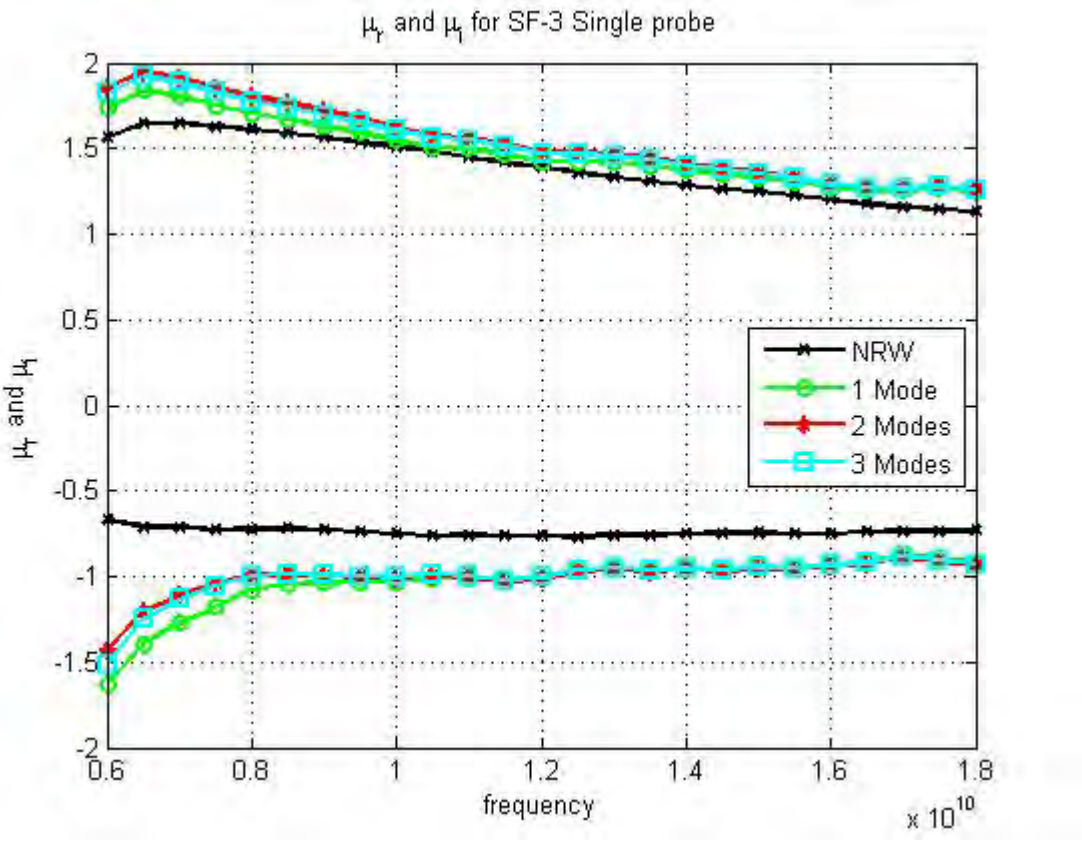


Figure 3.4: Calculated $\mu$ values for 1 - 3 modes as well as experimental results using a NRW method.

Figures 3.3 and 3.4 show that $\epsilon$ and $\mu$ calculations using multiple modes are consistent with those using a single mode. They are also consistent with the results using the NRW method. The small differences in results can be attributed to measurement errors and sample inconsistency. While using higher modes appears to yield a better result (converges closer to the NRW method) for some frequencies this is not the case in all of the frequencies. This leads to the conclusion that adding higher order modes when calculating $\epsilon$ and $\mu$ does not yield a significant benefit over using a single mode. This also proves that for this particular system, higher order modes are not being excited. If they are being excited, the amount of energy coupling is extremely low. This conclusion is confirmed by

examining the expected reflection coefficients for each mode. These expected coefficients (calculated with equations 3.21 and 3.22) are shown in Table 3.1, and show that the amount of energy reflected in the second and third mode are 1 and 2 orders of magnitude lower than that of the dominant mode.

Table 3.1: Expected reflection coefficients for each mode

| Mode | $\|\Gamma_1\|$ | $\|\Gamma_2\|$ |
|---|---|---|
| 1 | .3536 | .5265 |
| 2 | .0299 | .0369 |
| 3 | .0026 | .0017 |

Upon consideration of the findings in Figures 3.3 and 3.4, as well as Table 3.1, it is concluded that higher order modes do not need to be used for this class of materials to calculate accurate material parameters. Only needing a single mode will save valuable time and resources, and will yield a valuable diagnostic tool.

# IV. Multimode Clamped Probe DRWG

In this chapter, the analysis of a clamped probe DRWG, shown in Figure 4.1, is performed. The analysis includes an examination of the reflection and transmission coefficients of a lossy material sandwiched between two DRWGs. It is assumed in the analysis that only a single dominant mode is propagating in the free-space filled DRWG's however, higher order evanescent modes are allowed to exist during the analysis. The fundamental goal for performing this analysis is to assess if a single mode is sufficient to accurately determine permittivity and permeability of the material, or whether higher order modes must be included in the analysis to obtain accurate permittivity and permeability results. This answer will greatly impact the ability to perform these measurements in real time, versus needing a large amount of time to post-process.

The multimode clamped probe DRWG analysis uses the same field expressions detailed in chapter 2. First field expressions in the DRWG's are defined. Next, the fields in the PP region of the clamped probe DRWG are found with the aid of Love's Equivalence Theorem. Subsequent enforcement of tangential boundary conditions at the clamped probe DRWG apertures leads to coupled MFIE's for the unknown reflection and transmission coefficients. These MFIE's are solved via the Method-of-Moments for a lossy material. Experimental results for the calculation of $\epsilon_r$ and $\mu_r$ are presented and discussed, and general conclusions are provided.

## 4.1 Clamped Probe DRWG Region Fields

As a wave travels down the first DRWG and interacts with the boundary between the waveguide and the MUT, a portion of the energy will be reflected back into the waveguide [5]. Energy will also be transmitted through the PP region and into the second waveguide. Thus we must first find the total fields in the DRWG regions. All fields in a clamped probe

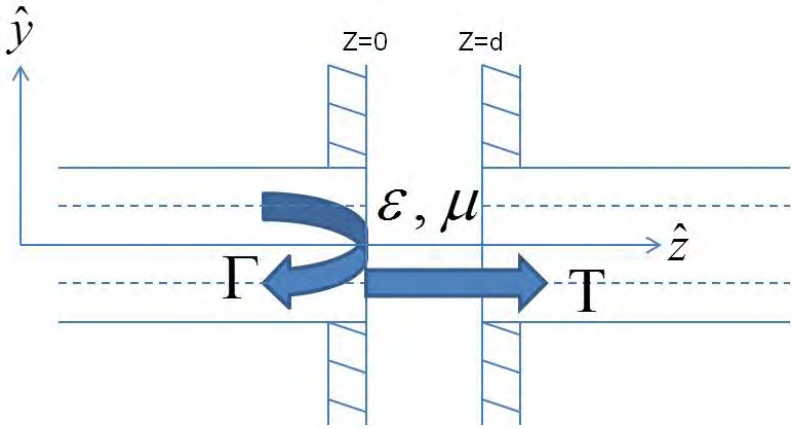


Figure 4.1: Side view of clamped probe DRWG geometry

DRWG system are found using a process similar to that used in chapter 2. Total fields in the DRWG portions of the system are found using the DRWG fields developed in chapter 2. While chapter 2 only uses a single mode, a more robust multi-mode analysis allows for multiple reflection and transmission coefficients for many potential waveguide modes. Allowing for this yields fields in the form of

$$\vec{E}_{DRWG1} = e^{-jk_z z}\vec{e}_{t1}(\vec{\rho}) + \sum_{q=1}^{N} \Gamma_q e^{jk_z z}\vec{e}_{tq}(\vec{\rho}) \tag{4.1}$$

$$\vec{H}_{DRWG1} = e^{-jk_z z}\vec{h}_{t1}(\vec{\rho}) - \sum_{q=1}^{N} \Gamma_q e^{jk_z z}\vec{h}_{tq}(\vec{\rho}) \tag{4.2}$$

$$\vec{E}_{DRWG2} = \sum_{q=1}^{N} \mathrm{T}_q e^{-jk_z(z-d)}\vec{e}_{tq}(\vec{\rho}) \tag{4.3}$$

$$\vec{H}_{DRWG2} = \sum_{q=1}^{N} \mathrm{T}_q e^{-jk_z(z-d)}\vec{h}_{tq}(\vec{\rho}) \tag{4.4}$$

where

$$\vec{e}_t = \hat{x}E_x + \hat{y}E_y \tag{4.5}$$

$$\vec{h}_t = \frac{\hat{z}\times\vec{e}_t}{Z^{TE}}. \tag{4.6}$$

Variable $\Gamma_q$ is the reflection coefficient associated with the $q^{th}$ even mode, and $T_q$ is the transmission coefficient associated with the $q^{th}$ even mode. Only even modes are considered because the dominant mode is even symmetric and the system is even symmetric. This forces all possible excited modes to be even. Variable $N$ is the number of modes allowed to be reflected and transmitted and can be as small or large as required for convergence. Upon inspection it is easy to see that equations 4.1 and 4.2 simplify to an equation similar to that of 2.6 and 2.7 if $N = 1$ and only one reflected mode is considered.

## 4.2 Parallel Plate Region Fields

As a wave travels down the first DRWG and contacts the interface between the waveguide and the MUT, a portion of the energy will be transmitted into the MUT. This energy gives rise to electromagnetic fields inside the PP region of the system. These fields are found using a process similar to that used in chapter 2. First Love's equivalence principle [5] is used to replace the actual sources (the DRWG apertures) with equivalent sources in the form of magnetic surface currents, namely [5]

$$\overrightarrow{M}_1 = -\hat{n} \times \overrightarrow{E}_1. \tag{4.7}$$

$$\overrightarrow{M}_2 = -\hat{n} \times \overrightarrow{E}_2. \tag{4.8}$$

where $\hat{n}$ the normal unit vector points into the MUT region. Note that $\hat{n}$ points in the positive $z$ direction for 4.7 and the negative $z$ direction for 4.8. This equivalent system is shown in Figure (4.2).

Now that the equivalent currents have been identified, a VP solution is used to find the parallel plate region fields. This solution is as follows:

$$\overrightarrow{H}_t^{pp}(\overrightarrow{\rho}, z) = \frac{1}{j\omega\epsilon\mu}(k^2 \underline{I}_t + \nabla_t \nabla \cdot) \overrightarrow{F}_t^{pp}(\overrightarrow{\rho}, z). \tag{4.9}$$

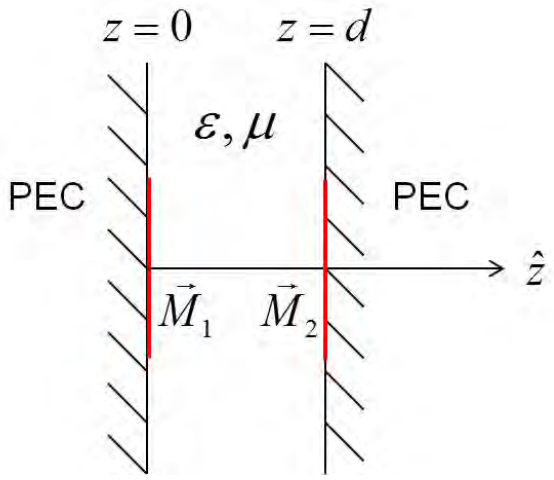


Figure 4.2: Equivalent system for parallel plate region of the clamped probe DRWG system after Love's Equivalence Theorem is applied.

However, the $\overrightarrow{F}$ VP must first be identified. The surface currents $\overrightarrow{M}_1$ and $\overrightarrow{M}_2$ support this vector through the following relation,

$$\overrightarrow{F}_t^{pp}(\overrightarrow{\rho},z) = \iint_{S_1} \underline{G}_1(\overrightarrow{\rho},z|\overrightarrow{\rho}',0)\cdot\epsilon\overrightarrow{M}_1(\overrightarrow{\rho}')ds' + \iint_{S_2} \underline{G}_2(\overrightarrow{\rho},z|\overrightarrow{\rho}',d)\cdot\epsilon\overrightarrow{M}_2(\overrightarrow{\rho}')ds' \quad (4.10)$$

where $\underline{G}_1(\overrightarrow{\rho},z|\overrightarrow{\rho}',0)$ and $\underline{G}_2(\overrightarrow{\rho},z|\overrightarrow{\rho}',d)$ are the parallel plate Green's functions associated with $\overrightarrow{M}_1$ and $\overrightarrow{M}_2$ respectively, and $\overrightarrow{M}_1$ and $\overrightarrow{M}_2$ are found using equation 4.7 and 4.8. Equating the tangential magnetic field at the apertures leads to the MFIEs

$$\frac{1}{j\omega\epsilon\mu}(k^2\underline{I}_t + \nabla_t\nabla\cdot)\overrightarrow{F}_t^{pp}(\overrightarrow{\rho},z) = \overrightarrow{h}_{t1}(\overrightarrow{\rho}) - \sum_{q=1}^{N}\Gamma_q\overrightarrow{h}_{tq}(\overrightarrow{\rho}). \quad (4.11)$$

$$\frac{1}{j\omega\epsilon\mu}(k^2\underline{I}_t + \nabla_t\nabla\cdot)\overrightarrow{F}_t^{pp}(\overrightarrow{\rho},z) = \sum_{q=1}^{N}\mathrm{T}_q\overrightarrow{h}_{tq}(\overrightarrow{\rho}) \quad (4.12)$$

These MFIEs are solved in the next section via the MoM.

### 4.3 Solving the MFIEs

This section details solving the MFIEs of the previous section. The first step of the MoM is to expand the unknown currents $(\overrightarrow{M}_1)$ and $(\overrightarrow{M}_2)$ as a series of basis functions. In

this case we will exploit the fact that we know the fields in the DRWG region just to the outside of the boundaries, and we know that these fields must be continuous across the boundaries, namely

$$\overrightarrow{M}_1(\overrightarrow{\rho}') = -\hat{n} \times \overrightarrow{E}_1 \approx -\hat{n} \times \overrightarrow{E}_{DRWG1}. \tag{4.13}$$

$$\overrightarrow{M}_2(\overrightarrow{\rho}') = -\hat{n} \times \overrightarrow{E}_2 \approx -\hat{n} \times \overrightarrow{E}_{DRWG2}. \tag{4.14}$$

Substituting 4.13 and 4.14 into 4.10 and further substituting into 4.11 and 4.12 yields the following relations after expansion:

$$\frac{1}{j\omega\mu}(k^2 \underline{I}_t + \nabla_t \nabla \cdot) \left[ \iint_{S_1} \underline{G}_1(\overrightarrow{\rho}, z|\overrightarrow{\rho}', 0) \cdot \overrightarrow{M}_1(\overrightarrow{\rho}') ds' + \iint_{S_2} \underline{G}_2(\overrightarrow{\rho}, z|\overrightarrow{\rho}', d) \cdot \overrightarrow{M}_2(\overrightarrow{\rho}') ds' \right] = \overrightarrow{h}_{t1}(\overrightarrow{\rho}) - \sum_{q=1}^{N} \Gamma_q \overrightarrow{h}_{tq}(\overrightarrow{\rho}) \tag{4.15}$$

$$\frac{1}{j\omega\mu}(k^2 \underline{I}_t + \nabla_t \nabla \cdot) \left[ \iint_{S_1} \underline{G}_1(\overrightarrow{\rho}, z|\overrightarrow{\rho}', 0) \cdot \overrightarrow{M}_1(\overrightarrow{\rho}') ds' + \iint_{S_2} \underline{G}_2(\overrightarrow{\rho}, z|\overrightarrow{\rho}', d) \cdot \overrightarrow{M}_2(\overrightarrow{\rho}') ds' \right] = \sum_{q=1}^{N} \mathrm{T}_q \overrightarrow{h}_{tq}(\overrightarrow{\rho}) \tag{4.16}$$

Next both sides of equations 4.15 and 4.16 are tested with $N$ total magnetic field modes. This must be done $N$ times because there are $N$ unknowns in each equation in the form of $\Gamma_1$ through $\Gamma_N$ and $\mathrm{T}_1$ through $\mathrm{T}_N$. The testing operators are as follows:

$$\iint_{S_1} \{\cdots\} \cdot \overrightarrow{h}^*_{t\tilde{q}} dS_1 \tag{4.17}$$

$$\iint_{S_2} \{\cdots\} \cdot \overrightarrow{h}^*_{t\tilde{q}} dS_2 \tag{4.18}$$

for 4.15 and 4.16 respectively. After testing 4.15 and 4.16 become

$$\iint_{S_1}\left(\frac{1}{j\omega\mu}(k^2\underline{I}_t+\nabla_t\nabla\cdot)\left[\iint_{S_1}\underline{G}_1(\vec{\rho},z|\vec{\rho}',0)\cdot\vec{M}_1(\vec{\rho}')ds'+\iint_{S_2}\underline{G}_2(\vec{\rho},z|\vec{\rho}',d)\cdot\vec{M}_2(\vec{\rho}')ds'\right]\right)\cdot\vec{h}^*_{t\tilde{q}}dS_1 = \iint_{S_1}\left(\vec{h}_{t1}(\vec{\rho})-\sum_{q=1}^{N}\Gamma_q\vec{h}_{tq}(\vec{\rho})\right)\cdot\vec{h}^*_{t\tilde{q}}dS_1 \tag{4.19}$$

$$\iint_{S_2}\left(\frac{1}{j\omega\mu}(k^2\underline{I}_t+\nabla_t\nabla\cdot)\left[\iint_{S_1}\underline{G}_1(\vec{\rho},z|\vec{\rho}',0)\cdot\vec{M}_1(\vec{\rho}')ds'+\iint_{S_2}\underline{G}_2(\vec{\rho},z|\vec{\rho}',d)\cdot\vec{M}_2(\vec{\rho}')ds'\right]\right)\cdot\vec{h}^*_{t\tilde{q}}dS_2 = \iint_{S_2}\left(\sum_{q=1}^{N}\mathrm{T}_q\vec{h}_{tq}(\vec{\rho})\right)\cdot\vec{h}^*_{t\tilde{q}}dS_2 \tag{4.20}$$

From this point forward it is desirable to work with a spectral representation of the Green's function. The Green's functions are shown below

$$\underline{G}_1(\vec{\rho},z|\vec{\rho}',0)=\frac{1}{(2\pi)^2}\iint_{-\infty}^{\infty}\widetilde{\underline{G}_1}(\vec{\lambda},z|0)e^{j\xi(x-x'_1)}e^{j\eta(y-y'_1)}d\xi d\eta \tag{4.21}$$

$$\underline{G}_2(\vec{\rho},z|\vec{\rho}',d)=\frac{1}{(2\pi)^2}\iint_{-\infty}^{\infty}\widetilde{\underline{G}_2}(\vec{\lambda},z|d)e^{j\xi(x-x'_1)}e^{j\eta(y-y'_1)}d\xi d\eta \tag{4.22}$$

where

$$\widetilde{\underline{G}_1}(\vec{\lambda},z|0)=\underline{I}_t\frac{\cosh(pd)}{p\sinh(pd)} \tag{4.23}$$

$$\widetilde{\underline{G}_2}(\vec{\lambda},z|d)=\underline{I}_t\frac{1}{p\sinh(pd)} \tag{4.24}$$

and

$$p=\sqrt{\xi^2+\eta^2-k^2}. \tag{4.25}$$

After using this Green's functions, rearranging the order of integration, and pulling out constants, equations 4.19 and 4.20 become

$$\begin{aligned}
&\frac{1}{j\omega\mu(2\pi)^2}\iint_{-\infty}^{\infty}\iint_{S_1} e^{j\xi x}\, e^{j\eta y} \\
&\Bigg[\iint_{S_1} e^{-j\xi x'}\, e^{-j\eta y'}\left((k^2\underline{I}_t + \nabla_t\nabla\cdot)\,\widetilde{\underline{G}_1}(\vec{\lambda}, z|0)\cdot\left(-\hat{n}\times\vec{E}_{DRWG1}\right)\right) \\
&+\iint_{S_2} e^{-j\xi x'}\, e^{-j\eta y'}\left((k^2\underline{I}_t + \nabla_t\nabla\cdot)\,\widetilde{\underline{G}_2}(\vec{\lambda}, z|0)\cdot\left(-\hat{n}\times\vec{E}_{DRWG2}\right)\right)\Bigg] \\
&\cdot\vec{h}^{\,*}_{t\tilde{q}}\, ds'\, ds\, d\eta\, d\xi \\
&= \iint_{S_1}\left(\vec{h}_{t1}(\vec{\rho}) - \sum_{q=1}^{N}\Gamma\vec{h}_{tq}(\vec{\rho})\right)\cdot\vec{h}^{\,*}_{t\tilde{q}}\, dS_1.
\end{aligned} \tag{4.26}$$

$$\begin{aligned}
&\frac{1}{j\omega\mu(2\pi)^2}\iint_{-\infty}^{\infty}\iint_{S_2} e^{j\xi x}\, e^{j\eta y} \\
&\Bigg[\iint_{S_1} e^{-j\xi x'}\, e^{-j\eta y'}\left((k^2\underline{I}_t + \nabla_t\nabla\cdot)\,\widetilde{\underline{G}_1}(\vec{\lambda}, z|0)\cdot\left(-\hat{n}\times\vec{E}_{DRWG1}\right)\right) \\
&+\iint_{S_2} e^{-j\xi x'}\, e^{-j\eta y'}\left((k^2\underline{I}_t + \nabla_t\nabla\cdot)\,\widetilde{\underline{G}_2}(\vec{\lambda}, z|0)\cdot\left(-\hat{n}\times\vec{E}_{DRWG2}\right)\right)\Bigg] \\
&\cdot\vec{h}^{\,*}_{t\tilde{q}}\, ds'\, ds\, d\eta\, d\xi \\
&= \iint_{S_2}\left(\sum_{q=1}^{N}\mathrm{T}_q\vec{h}_{tq}(\vec{\rho})\right)\cdot\vec{h}^{\,*}_{t\tilde{q}} dS_2
\end{aligned} \tag{4.27}$$

Once all operations are conducted on 4.26 and 4.27, a series of six dimensional integrals remain on the left of the equalities, and a double integral remains on the right of the equalities. The double integral on the right has three sections that must be calculated separately, one for each region of the waveguide. These integrals are straightforward and easily calculated using standard trigonometric identities and integration of trigonometric functions. Note these integrals must be calculated $N$ times due to there being $N$ unknowns. Because the waveguide modes are orthogonal only values where expansion and testing indices are equal ($q = \tilde{q}$) need to be calculated. The left side integrals are more complicated. In the clamped probe system 64 total 6 dimensional integrals must be calculated for each

combination of $q$ and $\tilde{q}$ leading to a total of $N^2\times$ 64 six dimensional integrals. An example of one of these integrals can be seen in chapters 2 and 3.

In these integrals the integration over spacial variables $(x, x', y, y')$ are easily computed using trigonometric identities and integration of trigonometric functions. However, integrals over spectral variables $(\xi, \eta)$ are more complicated. The integral over $\eta$ can be computed relatively easily using complex plane analysis (i.e. Cauchy's theorem). For more information on complex plane integration see chapter 2. Once all $\eta$ integrals are computed the $\xi$ integrals are computed numerically. These integrals contain branch cuts and cannot be found in closed form. MATLAB was used for all code and simulations for this research. Gaussian quadrature was used to integrate all $\xi$ integrals. Once all $\xi$ integrals are calculated a linear system of equations remains where $\Gamma_1$ through $\Gamma_N$ and $\mathrm{T}_1$ through $\mathrm{T}_N$ are the unknowns. This system can be rearranged such that:

$$\begin{bmatrix} a_{1,1} & \cdots & \cdots & \cdots & \cdots & a_{1,2N} \\ \vdots & \ddots & & & & \vdots \\ \vdots & & \ddots & & & \vdots \\ \vdots & & & \ddots & & \vdots \\ \vdots & & & & \ddots & \vdots \\ a_{2N,1} & \cdots & \cdots & \cdots & \cdots & a_{2N,2N} \end{bmatrix} \begin{bmatrix} \Gamma_1 \\ \vdots \\ \Gamma_N \\ \mathrm{T}_1 \\ \vdots \\ \mathrm{T}_N \end{bmatrix} = \begin{bmatrix} b_1 \\ \vdots \\ \vdots \\ \vdots \\ \vdots \\ b_{2N} \end{bmatrix}. \tag{4.28}$$

It is important to note that although there are multiple unknowns in equation 4.28, these values are not typically measurable. Only $\Gamma_1$ and $\mathrm{T}_1$ are typically measured since they represent reflection and transmission of the dominant propagating mode. Unlike the single probe, no more calculations need to be made as $\Gamma_1$ and $\mathrm{T}_1$ are two independent measurements.

## 4.4 Calculating $\epsilon$ and $\mu$

Now that all calculations needed to obtain and solve equation 4.28 are complete, material parameters $\epsilon$ and $\mu$ can be computed. In this step these parameters are solved iteratively using a least squares technique. First an initial guess for $\epsilon$ and $\mu$ is used to calculate initial $\Gamma_1$ and $T_1$ estimates. These estimates are compared to experimental measurements taken from a clamped probe system. Experimental measurement data used was the same data obtained and used in [20]. After comparing $\Gamma_1$ and $T_1$ to reflection and transmission coefficients of the experimental system, an update to $\epsilon$ and $\mu$ is calculated and used to recalculate $\Gamma_1$ and $T_1$. This process happens repeatedly until the difference in $\Gamma_1^1$ and $T_1$ and the experimental data is within tolerances set by the user. Broyden's Method was used to perform the iterative least squares operation. Experimental results of this process are shown in the next section.

## 4.5 ECCOSORB SF-3 Experimental Results

This section details the experimental results using multiple modes for the clamped probe DRWG system. All experimental data came from [20], see this for more details on the experimental setup and equipment used. In this experiment, material characterization measurements were made at 6-18 GHz of a lossy silicon-based magnetic absorbing material ECCOSORB SF-3 [16] manufactured by Emerson & Cuming Microwave Products, Inc. Figures 4.3 and 4.4 show calculated $\epsilon$ and $\mu$ values for SF-3 respectively. Both figures show calculations for 1 through 5 modes, and also show experimental results using a NRW method [22].

Figures 4.3 and 4.4 show that $\epsilon$ and $\mu$ calculations using multiple modes are consistent with those using a single mode for both MUTs. They are also consistent with the results using the NRW method. The small differences in results can be attributed to measurement errors and sample inconsistency. While using higher modes appears to yield a better result

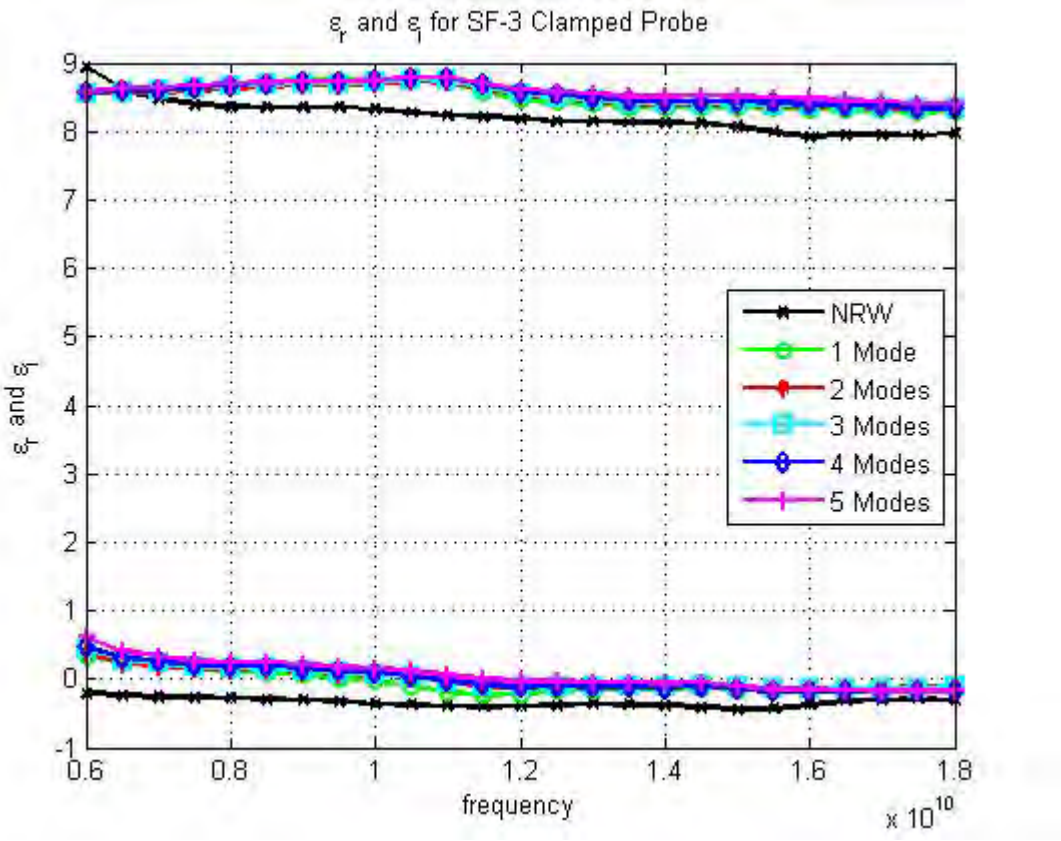


Figure 4.3: Calculated $\epsilon$ values of a clamped DRWG system with SF-3 MUT for 1 - 5 modes as well as experimental results using a NRW method.

(converges closer to the NRW method) for some frequencies this is not the case in all of the frequencies. This leads to the conclusion that adding higher order modes when calculating $\epsilon$ and $\mu$ does not yield a significant benefit over using a single mode. This also proves that for this particular system, higher order modes are not being excited. If they are being excited, the amount of energy coupling is extremely low. This conclusion is confirmed by examining the expected reflection and transmission coefficients for each mode. These expected coefficients (calculated with equation 4.28) are shown in Table 4.1, and show that the amount of energy reflected and transmitted in the higher modes is 1 to 2 orders of magnitude lower than that of the dominant mode.

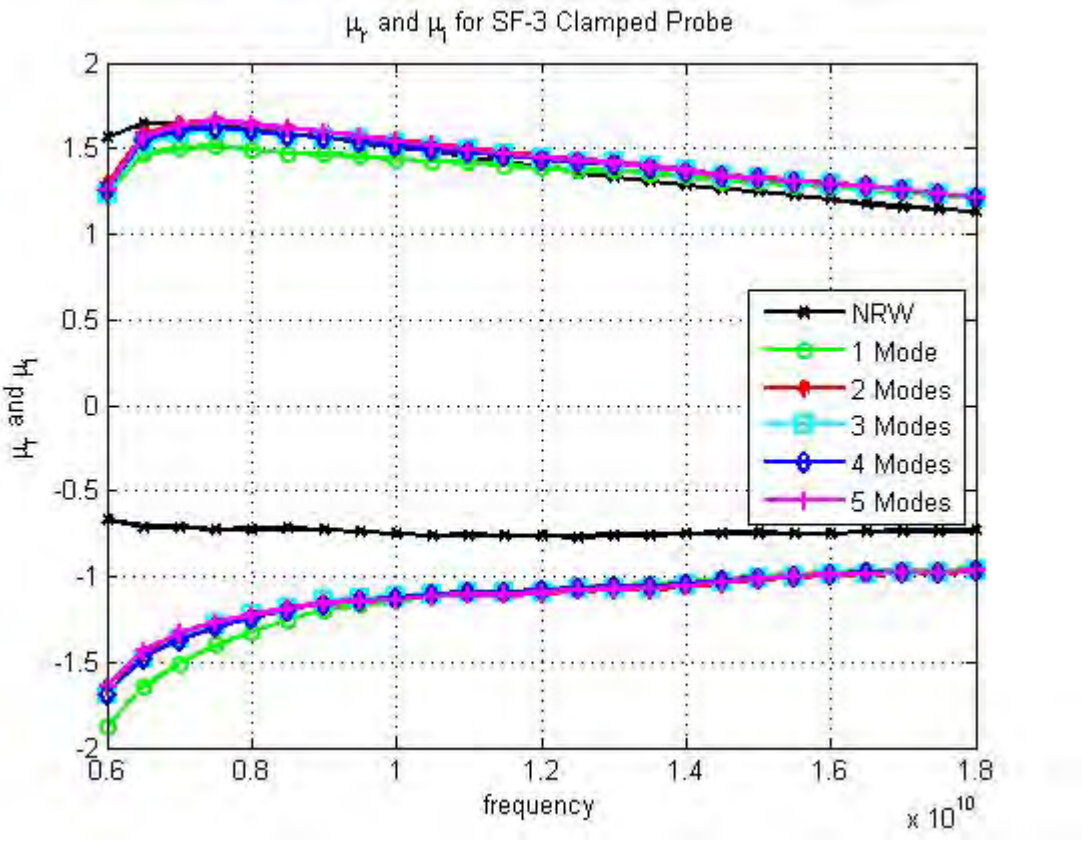


Figure 4.4: Calculated $\mu$ values of a clamped DRWG system with SF-3 MUT for 1 - 5 modes as well as experimental results using a NRW method.

Table 4.1: Expected reflection and transmission coefficients for each mode

| Mode | $\|\Gamma_1\|$ | $\|T\|$ |
|---|---|---|
| 1 | .6851 | .4230 |
| 2 | .0107 | .0199 |
| 3 | .0012 | .0005 |
| 4 | .0054 | .0021 |
| 5 | .0011 | .0009 |

Upon consideration of the findings in Figures 4.3 and 4.4, as well as Table 4.1, it is concluded that higher order modes do not need to be used for this class of materials to calculate accurate material parameters. Only needing a single mode will save valuable time and resources, and will yield a valuable diagnostic tool. These results are consistent to those found using the single probe DRWG system.

# V. Conclusion and Future Work

This chapter recaptures all work presented, and details the results as well as presents possible future research.

## 5.1 Dual Probe DRWG

In chapter 2 a dual probe DRWG system was analyzed. Dual probe systems have the ability to electromagnetically characterize PEC backed materials while taking both reflection and transmission measurements simultaneously. Previous DRWG research for PEC back material focused on a single probe system which required a two thickness technique to determine both permittivity and permeability. In some cases a two thickness technique may not be possible. This research removes that requirement and also saves setup time since a second setup is not required to obtain a second measurement.

Electromagnetic fields inside a dual probe DRWG system were presented. Fields in the PP region of the system were derived, and the resulting MFIE was solved using the MoM. Simulations were conducted to determine expected reflection and transmission coefficients for the system. The simulations showed realistic results. Another simulation was conducted to determine if the physical minimum distance between the two waveguides of the dual probe system was close enough to allow for a meaningful transmission measurement when using lossy material. It concluded that the transmission would indeed be measurable for lossy material. A final simulation was conducted using low loss material. This simulation showed that the transmission coefficient does not decay as fast as it does in the case of lossy material. This allows for more freedom when specifying the spacing between the DRWG's. Both simulations for lossy and low loss material exhibited oscillation in the measurements. This oscillation is attributed to constructive and destructive coupling between the DRWG's.

## 5.2 Multimode Single and Clamped Probe DRWG Systems

In chapters 3 and 4 electromagnetic fields inside a single probe DRWG system and clamped probe DRWG system were presented where higher order evanescent modes were allowed to exist. Fields in the PP region of the systems were derived, and the resulting MFIE's were solved using the MoM. A two thickness method was used to generate two independent measurements in the single probe system. In order to solve for permittivity and permeability, theoretical reflection and transmission measurements were compared to experimental reflection and transmission measurements. An iterative least squares technique was then used to determine permittivity and permeability.

Results for permittivity and permeability calculations using multiple higher order modes was presented and compared to results using only the dominant mode. While results for higher order modes and the dominant only mode were consistent, ultimately it was found that adding higher order modes to the analysis does not appear to increase overall accuracy in the single probe or clamped probe systems. This conclusion was determined by comparing these results to results gathered for the same material using a NRW method. Slight differences in material parameter calculation were attributed to measurement errors and material inconsistencies. Finally the expected reflection and transmission coefficients for higher order modes were used to confirm that these higher order modes are not being excited with enough energy to influence the resulting material parameter calculations.

## 5.3 Future Work

This research has answered two important questions. Is there sufficient coupling between waveguides in a dual probe DRWG system to be used to characterize lossy material parameters? Does including higher order modes in the analysis of DRWG systems increase the accuracy of material parameter calculations? While these answers are significant, many more questions in regards to DRWG systems have yet to be answered. A list of several potential topics for future research is presented here.

- In this research, only simple media was used for the analysis and experimental measurements. While this work is beneficial, many materials used in electromagnetic systems do not share all of these properties. Many materials used are anisotropic where permittivity and permeability of the material is dependent on the orientation of the incident electromagnetic field. Attempting to analyze anisotropic material is more difficult because these properties cannot be simplified to a single scalar value. The resulting permittivity and permeability matrices make analysis of DRWG systems more difficult. However, DRWG systems should be evaluated for potential use in characterizing anisotropic materials. It is recommended that this research start with only including a dominant mode reflection and transmission coefficient for simplicity. However, it would also be beneficial to investigate whether the addition of complex media necessitates the use of higher order modes for accurate material parameter calculation.

- In this research, DRWG's were used based on their broadband characteristics. Other waveguide shapes may exist which could keep the broadband operation of the DRWG yet allow for higher energy coupling in the dual probe system. Such examples include a system in which a single DRWG is used, along with a compliment shaped waveguide, or a system of two half trough ridged waveguides.

- In this research, differences in material parameter calculation were attributed to measurement errors and sample inconsistencies. While these are reasonable conclusions, it would be beneficial to study the effects of errors on the multimode DRWG systems. A full error analysis would also yield higher confidence in these calculations.

- In this research, the dual probe system was shown to be capable of calculating material parameters for low loss media. However, because reflection and transmission

coefficients do not decay very fast with low loss media, it is possible to have the DRWG's farther apart and still take meaningful measurements. It was also noted that the optimal placement of waveguides could change as operating frequency changes. Thus, it would be beneficial to further study how the dual probe system operates with low loss material, as well as how error varies with DRWG spacing.

## Bibliography


[1] Arfken, Hans J; Harris Frank E, George B; Weber. *Mathematical Methods for Physicists*. Elsevier Inc, 2013.

[2] Baker-Jarvis, James and Michael D Janezic. "Analysis of a two-port flanged coaxial holder for shielding effectiveness and dielectric measurements of thin films and thin materials". *Electromagnetic Compatibility, IEEE Transactions on*, 38(1):67–70, 1996.

[3] Baker-Jarvis, James, Michael D Janezic, Paul D Domich, and Richard G Geyer. "Analysis of an open-ended coaxial probe with lift-off for nondestructive testing". *Instrumentation and Measurement, IEEE Transactions on*, 43(5):711–718, 1994.

[4] Baker-Jarvis, James, Eric J Vanzura, William Kissick, et al. "Improved technique for determining complex permittivity with the transmission/reflection method". *Microwave Theory and Techniques, IEEE Transactions on*, 38(8):1096–1103, 1990.

[5] Balanis, Constantine A. *Advanced Engineering Electromagnetics*. Wiley New York, 2012.

[6] Bird, Trevor S. "Mutual coupling in arrays of coaxial waveguides and horns". *Antennas and Propagation, IEEE Transactions on*, 52(3):821–829, 2004.

[7] Bois, Karl J, Aaron D Benally, and Reza Zoughi. "Multimode solution for the reflection properties of an open-ended rectangular waveguide radiating into a dielectric half-space: The forward and inverse problems". *Instrumentation and Measurement, IEEE Transactions on*, 48(6):1131–1140, 1999.

[8] Boybay, Muhammed S and Omar M Ramahi. "Open-ended coaxial line probes with negative permittivity materials". *Antennas and Propagation, IEEE Transactions on*, 59(5):1765–1769, 2011.

[9] Chang, Chih-Wei, Kun-Mu Chen, and Jian Qian. "Nondestructive determination of electromagnetic parameters of dielectric materials at X-band frequencies using a waveguide probe system". *Instrumentation and Measurement, IEEE Transactions on*, 46(5):1084–1092, 1997.

[10] Chen, Chun-Ping, Zhewang Ma, Tetsuo Anada, and Jui-Pang Hsu. "Further study on two-thickness-method for simultaneous measurement of complex EM parameters based on open-ended coaxial probe". *Microwave Conference, 2005 European*, volume 1, 4–pp. IEEE, 2005.

[11] De Langhe, Pascal, Krist Blomme, Luc Martens, and Daniël De Zutter. "Measurement of low-permittivity materials based on a spectral-domain analysis for the open-ended coaxial probe". *Instrumentation and Measurement, IEEE Transactions on*, 42(5):879–886, 1993.

[12] De Langhe, Pascal, Luc Martens, and Daniël De Zutter. "Design rules for an experimental setup using an open-ended coaxial probe based on theoretical modelling". *Instrumentation and Measurement, IEEE Transactions on*, 43(6):810–817, 1994.

[13] Dester, Gary D, Edward J Rothwell, and Michael J Havrilla. "Two-iris method for the electromagnetic characterization of conductor-backed absorbing materials using an open-ended waveguide probe". *Instrumentation and Measurement, IEEE Transactions on*, 61(4):1037–1044, 2012.

[14] Dester, Gary Dean, Edward J Rothwell, Michael John Havrilla, and Milo Wilt Hyde IV. "Error analysis of a two-layer method for the electromagnetic characterization of conductor-backed absorbing material using an open-ended waveguide probe". *Progress In Electromagnetics Research B*, 26:1–21, 2010.

[15] Elliott, Robert Stratman. *An introduction to guide waves and microwave circuits*. Prentice-Hall, 1993.

[16] Emerson and Inc. Cuming Microwave Products. "ECCOSORB SF Thin, Flexible, Resonant Absorbers". *http://www.eccosorb.com/Collateral/Documents/English-US/SF.pdf*, 2007.

[17] Folgerø, Kjetil and Tore Tjomsland. "Permittivity measurement of thin liquid layers using open-ended coaxial probes". *Measurement Science and Technology*, 7(8):1164, 1996.

[18] Ganchev, Stoyan, Sasan Bakhtiari, Reza Zoughi, et al. "A novel numerical technique for dielectric measurement of generally lossy dielectrics". *Instrumentation and Measurement, IEEE Transactions on*, 41(3):361–365, 1992.

[19] Hyde, J. W. Stewart M. J. Havrilla W. P. Baker E. J. Rothwell, M. W. and D. P. Nyquist. "Nondestructive electromagnetic material characterization using a dual waveguide probe: a full wave solution". *Radio Science*, 44(3), 2009.

[20] Hyde, M. J. Havrilla, M. W. "A clamped dual-ridged waveguide measurement system for the broadband nondestructive characterization of sheet materials". *Radio Science*, 48(5), 2013.

[21] Hyde, M. J. Havrilla, M. W. "Broadband, non-destructive characterisation of PEC-backed materials using a dual-ridged-waveguide probe". *IET Science, Measurement and Technology*, 2014.

[22] Hyde, Milo W, Michael J Havrilla, Andrew E Bogle, and Nathan J Lehman. "Broadband characterization of materials using a dual-ridged waveguide". *Instrumentation and Measurement, IEEE Transactions on*, 62(12):3168–3176, 2013.

[23] Hyde, Milo W, James W Stewart, Michael J Havrilla, William P Baker, Edward J Rothwell, and Dennis P Nyquist. "Nondestructive electromagnetic material characterization using a dual waveguide probe: A full wave solution". *Radio Science*, 44(3), 2009.

[24] Hyde IV, Milo Wilt and Michael John Havrilla. "A nondestructive technique for determining complex permittivity and permeability of magnetic sheet materials using two flanged rectangular waveguides". *Progress In Electromagnetics Research*, 79:367–386, 2008.

[25] Li, Ching-Lieh and Kun-Mu Chen. "Determination of electromagnetic properties of materials using flanged open-ended coaxial probe-full-wave analysis". *Instrumentation and Measurement, IEEE Transactions on*, 44(1):19–27, 1995.

[26] Maode, Niu, Su Yong, Yan Jinkui, Fu Chenpeng, and Xu Deming. "An improved open-ended waveguide measurement technique on parameters ϵ $\gamma$ and $\mu$ $\gamma$ of high-loss materials". *Instrumentation and Measurement, IEEE Transactions on*, 47(2):476–481, 1998.

[27] Montgomery, James P. "On the Complete Eigenvalue Solution of Ridged Waveguide". *Microwave Theory and Techniques, IEEE Transactions on*, 19(6):547–555, 1971.

[28] N.V., Emerson Cuming Microwave Products. "ECCOSORB FGM-125". *http://www.eccosorb.eu/sites/default/files/techbulletins/eb*$_3$*21*$_f$*gm* − *125.pdf*, 2015.

[29] Olmi, R, M Bini, R Nesti, G Pelosi, and C Riminesi. "Improvement of the permittivity measurement by a 3D full-wave analysis of a finite flanged coaxial probe". *Journal of electromagnetic waves and applications*, 18(2):217–232, 2004.

[30] Rogers, Neil G. *Nondestructive Electromagnetic Characterization of Uniaxial Materials*. Air Force Institute of Technology, 9 2014.

[31] Sanadiki, Bassam, Masoud Mostafavi, et al. "Inversion of inhomogeneous continuously varying dielectric profiles using open-ended waveguides". *Antennas and Propagation, IEEE Transactions on*, 39(2):158–163, 1991.

[32] Shin, Dong H and Hyo J Eom. "Estimation of dielectric slab permittivity using a flared coaxial line". *Radio Science*, 38(2), 2003.

[33] Stewart, JW and MJ Havrilla. "Electromagnetic characterization of a magnetic material using an open-ended waveguide probe and a rigorous full-wave multimode model". *Journal of electromagnetic waves and applications*, 20(14):2037–2052, 2006.

[34] Tantot, Olivier, Michel Chatard-Moulin, and Pierre Guillon. "Measurement of complex permittivity and permeability and thickness of multilayered medium by an open-ended waveguide method". *Instrumentation and Measurement, IEEE Transactions on*, 46(2):519–522, 1997.

[35] Wang, Shoujun, Maode Niu, and Deming Xu. "A frequency-varying method for simultaneous measurement of complex permittivity and permeability with an open-ended coaxial probe". *Microwave Theory and Techniques, IEEE Transactions on*, 46(12):2145–2147, 1998.

[36] Wu, Mingzhong, Xi Yao, and Liangying Zhang. "An improved coaxial probe technique for measuring microwave permittivity of thin dielectric materials". *Measurement science and technology*, 11(11):1617, 2000.

# REPORT DOCUMENTATION PAGE

*Form Approved*
*OMB No. 0704–0188*



| 1. REPORT DATE *(DD–MM–YYYY)* | 2. REPORT TYPE | 3. DATES COVERED *(From — To)* |
|---|---|---|
| 17–09–2015 | Dissertation | Oct 2012–Sep 2015 |

**4. TITLE AND SUBTITLE**

Multi-Mode Analysis of
Dual Ridged Waveguide Systems
for Material Characterization

**5a. CONTRACT NUMBER**

**5b. GRANT NUMBER**

**5c. PROGRAM ELEMENT NUMBER**

**6. AUTHOR(S)**

Crosby, Jason G., Major, USAF

**5d. PROJECT NUMBER**

**5e. TASK NUMBER**

**5f. WORK UNIT NUMBER**

**7. PERFORMING ORGANIZATION NAME(S) AND ADDRESS(ES)**

Air Force Institute of Technology
Graduate School of Engineering and Management (AFIT/EN)
2950 Hobson Way
Wright-Patterson AFB, OH 45433-7765

**8. PERFORMING ORGANIZATION REPORT NUMBER**

AFIT-ENG-DS-15-S-011

**9. SPONSORING / MONITORING AGENCY NAME(S) AND ADDRESS(ES)**

Intentionally Left Blank

**10. SPONSOR/MONITOR'S ACRONYM(S)**

**11. SPONSOR/MONITOR'S REPORT NUMBER(S)**

**12. DISTRIBUTION / AVAILABILITY STATEMENT**

DISTRIBUTION STATEMENT A:
APPROVED FOR PUBLIC RELEASE; DISTRIBUTION UNLIMITED

**13. SUPPLEMENTARY NOTES**



**14. ABSTRACT**

In this dissertation, two nondestructive dual ridged waveguide (DRWG) material characterization systems are investigated. The single and clamped DRWG probe geometries were analyzed in previous work; however, that research only incorporated the dominant DRWG mode. Here, that restriction is removed and the existence of evanescent higher-order modes is considered. Theoretical analysis of the single and clamped DRWG probes is presented and discussed. The approach taken here is similar to that presented in previous research: Love's equivalence theorem is used to remove the DRWG apertures which are replaced with equivalent magnetic currents radiating in the presence of the background parallel-plate waveguide structure. Enforcing the continuity of the tangential magnetic fields in the DRWG and parallel-plate regions yields a system of coupled magnetic field integral equations (MFIEs). This coupled MFIE system is solved using the Method of Moments (MoM) where the tangential electric and magnetic fields in the DRWG are used as expansion and testing functions, respectively. Inversion of the resulting MoM impedance matrix produces theoretical expressions for the reflection and transmission coefficients which are numerically inverted (via nonlinear least squares) to yield estimates of the permittivity and permeability of the material under test. While the steps taken in the theoretical development are similar to previous work, the addition of higher-order modes into the analysis substantially complicates the derivation and is a significant extension of the existing dominant-mode-only literature. Lastly, simulation results of the two structures are presented. A comparison of the dominant-mode only reflection and transmission coefficients with the higher-order mode coefficients is provided.

**15. SUBJECT TERMS**

dual ridged waveguide, multi-mode, material characterization, clamped probe, dual probe

| 16. SECURITY CLASSIFICATION OF: | | | 17. LIMITATION OF ABSTRACT | 18. NUMBER OF PAGES | 19a. NAME OF RESPONSIBLE PERSON |
|---|---|---|---|---|---|
| a. REPORT | b. ABSTRACT | c. THIS PAGE | | | Dr. Michael J. Havrilla (ENG) |
| U | U | U | UU | 73 | 19b. TELEPHONE NUMBER *(include area code)* (937) 255-3636 x4582 michael.havrilla@afit.edu |